Chemical Engineering Journal 469 (2023) 144007

Contents lists available at ScienceDirect

Chemical Engineering Journal

journal homepage: www.elsevier.com/locate/cej

The role of AgNPs in selective oxidation of benzyl alcohol in vapor phase using morphologically tailored MnO_2 nanorods in the presence of air

Rajesh Rajendiran [a], Shrutika Lingalwar [a], Assa Aravindh [b], Alagusundari Karuppiah [c], Putrakumar Balla [d], Prem Kumar Seelam [e,*], B. Shanmugavelu [f], Vijayanand Perupogu [a,*], Sungtak Kim [d], Ulla Lassi [e]

[a] Energy & Environmental Engineering Department, CSIR-Indian Institute of Chemical Technology (IICT), Hyderabad 500007, India
[b] Nano and Molecular Systems (NANOMO) Research Unit, Faculty of Science, P.O. Box 4300, University of Oulu, Oulu 90014, Finland
[c] Department of Chemistry, Pondicherry Central University, Kalapet, Pondicherry 605014, India
[d] Department of Chemical Engineering and Applied Chemistry, Chungnam National University, Daejeon 34134, Republic of Korea
[e] Sustainable Chemistry Research Unit, Faculty of Technology, P.O. Box 4300, University of Oulu, Oulu 90014, Finland
[f] Department of Science (Physics), Sona College of Technology, Salem 636005, Tamil Nadu, India

ARTICLE INFO

Keywords:
Ag
Benzyl alcohol
MnO2 nanorods
Oxidation
Vapor phase

ABSTRACT

Vapor phase benzyl alcohol (BnOH) oxidation reaction is investigated over a pre–synthesised morphologically designed shape controlled spherical silver nanoparticles (AgNPs) decorated on manganese oxide nanorods (α–MnO_2NRs) in the presence of air. The combination of silver nanoparticles and the α–MnO_2NRs interface enabled the increased oxygen vacancies (O_v) and exhibited the strong metal–support interactions (SMSI) in surface oxygen activation. The effect of Ag loadings is significant and the optimal 1 wt% Ag loaded catalyst (1Ag/MnO_2NRs) showed excellent performance in benzyl alcohol oxidation due to high adsorption capacity, enhanced oxygen vacancies and red–ox properties. The DFT calculations confirmed that the high BnOH surface adsorption was exhibited over Ag modified MnO_2NRs than the bare α–MnO_2NRs. The optimized 1Ag/α–MnO_2NRs catalytic system achieved 2.6 fold higher activity compared to bare α–MnO_2NRs. These results provided novel insights on the rational design of shape dependent metal/metal oxide based heterogeneous catalysts.

1. Introduction

Catalytic oxidation of alcohols to its corresponding carbonyls is one of the important organic processes with respect to economic value and scientific interest and globally produced at a rate of>10 000 million tons per year in the 21st century [1–3]. The existing industrial oxidation process traditionally relied on the use of strong and stoichiometric oxidizing reagents such as permanganate, hypochlorite, or dichromate, etc., which are typically expensive and hazardous [3]. Additionally, the strength of these oxidizing agents can make alcohols to undergo total oxidation into CO_2 or carboxylic acids, thus, it reduces the aldehydes selectivity [4]. The alternative approach is to use the environmentally benign oxidants such as air and/or molecular O_2 [5].

A significant number of research has been dedicated to the liquid-phase aerobic oxidation of benzyl alcohol over different catalysts [6–12]. Nevertheless, there are challenges that exist with the liquid–phase method, such as difficulty in catalyst separation, metal leaching from the catalyst, poor heat and mass transfer rates. However, none of the aforementioned disadvantages exist related to the vapor phase method. Noticeable works are published on vapor phase BnOH oxidation reaction using noble (such as gold and silver) and non-noble metal (Co, Ni and Cu) based supported metal oxides and mixed metal oxides catalysts [13–22]. Recently active phase metals such as Au, Ag, and Cu-based catalysts received much attention in vapor–phase method. It has been demonstrated that the vapor–phase reactions can be catalysed at temperatures between 300 and 380 °C over Au and Ag–based catalysts [13–16,18]. Over AuCu/SiO_2 catalyst has been reported to achieve 98% benzaldehyde yield at 260 °C, which is significantly highest activity among the reported Au-based catalysts [23,24]. However, the expensive Au is not suitable for large scale industrial application. Similarly, Ag–based Ag–Ni fibre catalysts have also shown selectivity above 95% and conversion above 80%. However it requires higher temperatures (over 380 °C) to reach high activity and selectivity [16]. Moreover, it has been noted that number of transition non-noble metal–based catalysts

* Corresponding authors.
E-mail addresses: prem.seelam@oulu.fi (P.K. Seelam), pvanand@iict.res.in (V. Perupogu).

https://doi.org/10.1016/j.cej.2023.144007
Received 18 March 2023; Received in revised form 14 May 2023; Accepted 6 June 2023
Available online 8 June 2023

including Cu and Co based catalysts are active at higher temperatures between 300 and 400 °C [15,18,22]. Recently, it has been demonstrated that a mesoporous type catalytic system comprising of K, Cu, and TiO_2 materials exhibited outstanding properties which are active at low temperature (210 °C) vapor–phase benzyl alcohol oxidation reaction [15]. However, these catalysts exhibit low conversion rates at low weight hour space velocities (WHSVs) and it is extremely temperature-sensitive (>223 °C). Further, slightly at higher reaction temperature *i.e.,* above 247 °C resulted in the complete oxidation of benzyl alcohol to undesired benzoic acid, and exhibit low stability [15]. Similarly, mixed metal oxides such as MnO_2–CeO_2 shown promising results in vapor phase oxidation of BnOH than the bare MnO_2 oxide, however it has low reaction rate and poor stability issues when compared to metal/metal oxides catalysts [23].

Still there are challenges in designing and preparing a highly effective catalyst which is active at low temperatures and at moderate WHSVs. In order to design a most active and selective metal/metal oxide-based catalyst, modifying the crystal phase and the structure of the metal oxide might be the appropriate method. It is highly critical to investigate how different oxides, metals and other active interfaces might affect the BnOH oxidation activity. Among all transition metal oxides, manganese oxides (MnO_x) are the most suitable carrier material for oxidation reactions due to abundant, high oxygen storage capacity, tunable crystal phases, high oxide reduction rates, and high O_v formation at low temperatures [25–27]. Recently, Shi *et al*, studied the effect of different structures and crystal phases of MnO_2 *i.e.,* α, β, γ, δ–crystal structures and the activity of high surface area β(1 1 0) crystal phase exhibited highest BnOH conversion due to the high density of oxygen vacancies (O_v), O_v formation energies, and the unsaturated Mn sites [28]. This work gives a preliminary idea to understand the effect of MnO_2 crystal structure on BnOH oxidation reaction. However, the reaction rate of all the MnO_2 crystal structures (α, β, γ, and δ–crystals) are relatively low compared to metal/metal oxide catalysts.

The best way to enhance the catalytic performance is by selectively exposing reactive crystal facets on the surface of the metal and metal oxide particles interface by shape and size controlled synthesis. Moreover, the enrichment of active sites *via* electronic structure and surface coordination environment can be morphologically tailored. These significant modifications to the electronic structure and surface atomic configurations can modify the chemical and physical characteristics of heterogeneous catalysts, which in turn influence the overall activity and selectivity [29,30]. The previously reported studies on BnOH oxidation reaction using AgNPs presented very low reaction rates and poor stability in both liquid and vapor phase [13,15–16], it may be due to non-homogenous and bigger size AgNPs. In this work, we designed and synthesised highly novel and active spherical shaped Ag nanoparticles over shaped controlled α–MnO_2 nanorods supported nanocatalyst in partial oxidation of BnOH reaction. This is the first study on Ag NPs loaded α–MnO_2 nanocatalyst in BnOH oxidation and the activity of Ag/MnO_2 interface is well correlated under optimized conditions. This could be given the opportunity to achieve high catalytic performance over Ag/α–MnO_2NRs in the vapor phase BnOH oxidation in presence of air.

2. Experimental details

2.1. Chemicals

Sulfuric acid, potassium permanganate, manganese sulfate monohydrate, silver nitrate, dodecylamine, formaldehyde, ethanol, benzyl alcohol, benzaldehyde, were purchased from Sigma–Aldrich India.

2.2. Synthesis of spherical silver nanoparticles

A 6 g of dodecylamine were added to a 200 mL cyclohexane solution, which was then stirred for 30 min. Further, 10 mL of aqueous formaldehyde (37 vol%) were added to this homogeneous mixture. After washing with water, the organic phase was removed by using a separating funnel (2 × 200 mL). In the next step, $AgNO_3$ aqueous solution was added (1.6 g $AgNO_3$ in 80 mL H_2O) to this organic solution and stirred it for 12 h (Scheme 1). After separating the organic phase, 200 mL of ethanol was used to precipitate the AgNPs. The centrifuged AgNPs precipitate was collected and dissolved in small amount of cyclohexane (40 mL) [31].

2.3. Preparation of α–MnO_2NRs nanorods

By modifying our earlier method, the α–MnO_2 nanorods (NRs) were synthesized and presented in scheme 1 [32]. Manganese sulphate monohydrate ($MnSO_4$ H_2O) (3.165 g) and potassium permanganate ($KMnO_4$) (1.78 g) were first dissolved in 55 mL of water. Next, dropwise addition of sulfuric acid (98 wt%) 0.07 mol (~3.75 mL) was added in the solution. To obtain a homogenous solution, the mixture was further stirred for 10 min., and then it was then placed in autoclaved for 10 h at 150 °C. Double distilled water and ethanol were used to filter and wash the product. The final product was allowed to dry overnight at 50 °C under vacuum followed by calcination at 400 °C for 5 h under air (Scheme 1).

2.4. AgNPs deposition on α–MnO_2NRs

The α–MnO_2NRs were added after dispersing the pre-synthesised silver NPs (AgNPs) in cyclohexane and ethanol solutions. The resulting suspension was then sonicated for 5–10 min before stirring at 600 rpm with a magnetic stirrer overnight. After centrifugation, the sample was vacuum-dried at 50 ℃ for an overnight duration. And then it was calcined at 350 °C for five hours in air. The sample with nominal 0.5, 1, 1.5 and 2 wt% Ag loadings were prepared and denoted as 0.5Ag/α–MnO_2NRs, 1Ag/α–MnO_2NRs, 1.5Ag/α–MnO_2NRs and 2Ag/α–MnO_2NRs [32].

2.5. Ag(C)/MnO_2NRs synthesis (conventional method)

The required amount of α–MnO_2NRs dispersed in appropriate amount of $AgNO_3$ aqueous solution. This solution is allowed to stir in magnetic stirrer for 20 min at room temperature. Further, to this aqueous solution, $NaBH_4$ solution added drop wise in 1:1 M ratio with respect to $AgNO_3$. The resultant solution was allowed to be stirred for another 12 h. Final product was filtered and washed twice with double distilled water. The filtered solid product was vacuum-dried at 50 ℃ for an overnight duration. And then it was calcined at 350 °C for five hours in air. The catalyst is designated as Ag(C)/MnO_2NRs.

2.6. Materials characterization

The samples were digested with aqua regia in a microwave oven before being used to conduct the inductively coupled plasma optical emission spectroscopy (ICP-OES) analysis of the silver loading samples. The powder X–ray diffraction (XRD) analysis was performed on an X–ray diffractometer (Rigaku miniflex) to identify the crystalline nature of the catalysts. With a beam current of 15 mA and beam voltage of 30 kV, the analysis was performed at a scan rate of 2° min^{-1} using Ni–filtered Cu Kα radiation (λ = 0.15406 nm) from 2θ = 2° to 80°. Nitrogen adsorption–desorption isotherms (physisorption) at –196 °C were used to quantify the textural characteristics of the catalysts, such as the Brunauer–Emmet–Teller (BET) surface area, pore volume, and average pore diameter (using Quanta chrome instruments). The FTIR spectra were captured using the KBr background spectrum on the FT–IR Nicolet 670 spectrometer in the spectral range of 1400–1800 cm^{-1} was analysed. The Auto Chem 2910 apparatus (Micromeritics, USA) used for the oxygen temperature programmed desorption (O_2–TPD) experiments equipped with a TCD detector, which allowed to measure the desorbed

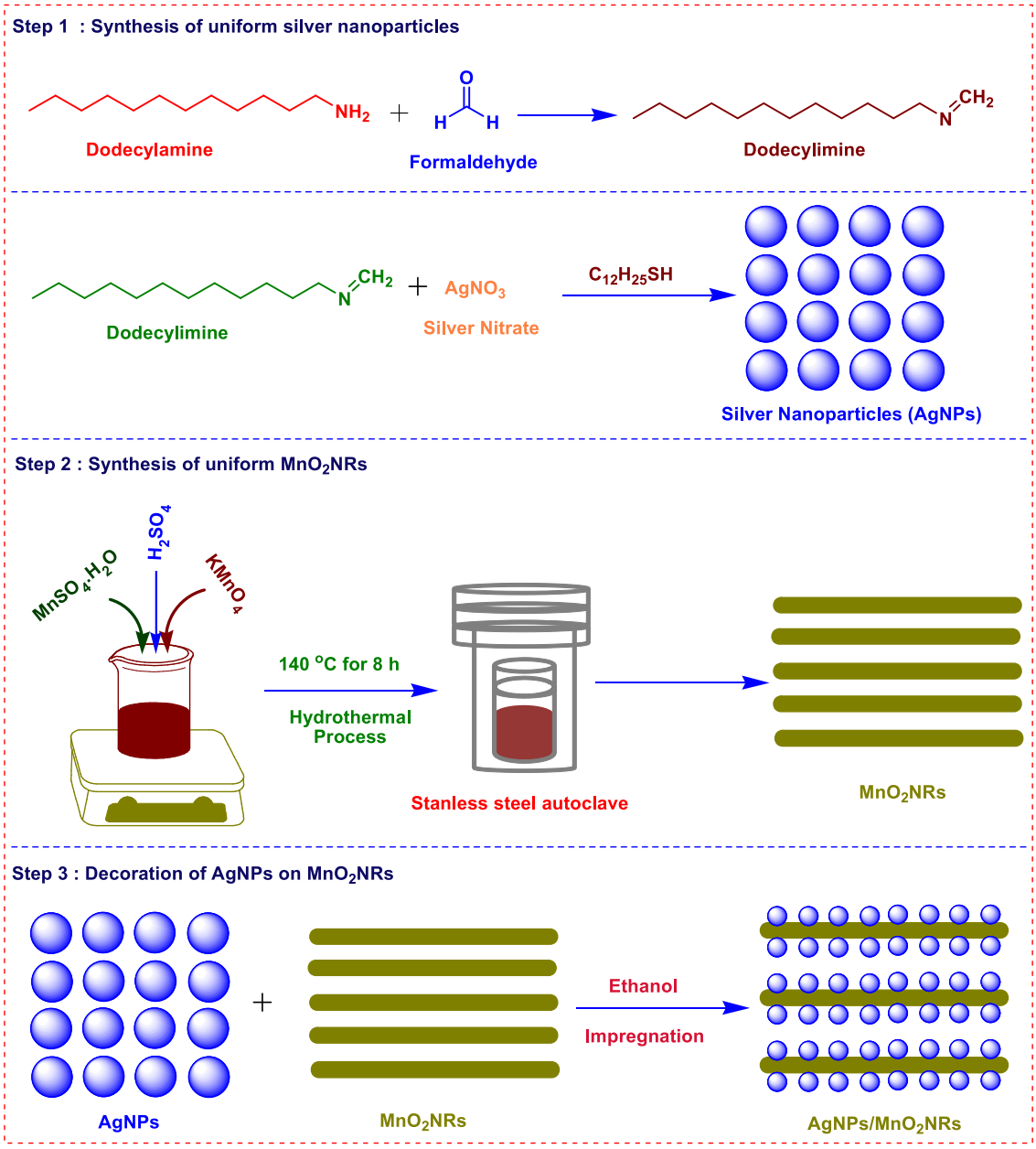

Scheme1. Schematic illustration of the stepwise formation of AgNPs over α–MnO_2NRs nanocatalyst. Step 1: Pre synthesised silver nanoparticles with controlled spherical shaped with ultra–fine size, step 2: formation of MnO_2NRs and step 3: decoration of AgNPs on MnO_2NRs surface.

O_2 from the sample by measuring continuously at elevated temperatures. Prior to the TPD measurements, 0.1 g of sample was dried under helium flow of 50 mL.min^{-1} at 200 °C for 1 h. The next step was to perform O_2 adsorption using a mixture of 10 vol% O_2/He to measureO_2–TPD profile at 80 °C for 1 h, or until saturation point was reached. Next, degassed for 30 min with an inert flow at 50 mL.min^{-1}. The TPD study was performed in the temperature range of 100 °C to 800 °C at a heating rate of 10 °C min^{-1}, and the GRAMS/32 software was used to measure the amount of desorbed O_2. An AutoChem 2920 (Micromeritics) device was used to perform the hydrogen temperature-programmed reduction (H_2–TPR) study. A 0.05 g sample was placed in a U–shaped quartz tube for the TPR tests. The catalyst was mounted on a quartz wool plug in the tube. The catalyst was pretreated with N_2 gas flow at a rate of 30 mL.min^{-1} for 1 h at 200 °C before the TPR experiment. After the pretreatment process, the sample was cooled to room temperature before the TPR tests. And then it was run under a 5 vol % H_2/He flow (30 mL.min^{-1}) and temperature ramping from 30 to 800 °C at a rate of 5 °C/min, loiter for a short period of time, and then continue until steady state was achieved. The H_2 consumption was then calculated based on the TPR peaks at various temperature zones after cooling down to RT (denoted as low, medium, and high temperature regions, respectively). Using a JEOL 2010 electron microscope instrument operating at 200 kV, TEM investigation was carried out. The catalyst was dispersed on ethanol and then it was loaded on a carbon-coated copper grid. The sample-containing specimen was placed inside the microscope column, which was subsequently evacuated at a pressure of 10^{-6} Torr. Using a Philips Fei Quanta 200F instrument operating at 20 kV, morphological and structural images were captured for scanning electron microscopy (SEM) investigation. An FEI Tecnai G2 F30S–Twin microscope operating at 300 kV was used to capture high resolution TEM (HRTEM) pictures. Thermo Scientific Multilab 2000 with Al K radiation (1486.6 eV) operating at 15 kV and 10 mA (150 W) was used to record the X-ray photoelectron spectra (XPS) of the α–MnO_2NRs and Ag/α–MnO_2NRs catalysts. The binding energies listed here refer to C 1 s at

284.5 eV. The powder samples were spread out on the conductive carbon tape and put into an ultrahigh vacuum (UHV) preparation chamber for XPS investigations in order to desorb any adsorbed species that might have been on the sample surface. The samples were sequentially moved with UHV to the analyser chamber after five hours. All spectra were recorded with pass energy of 30 eV and a step increase of 0.05 eV. By using a Witec Confocal Raman instrument (CRM200) and an Ar ion laser ($\lambda = 514.5$ nm), the Raman spectra of the synthesized α–MnO_2NRs and Ag/α–MnO_2NRs catalysts were measured. Diffuse reflectance infrared Fourier transform (DRIFT) analyses were performed by in situ benzyl alcohol oxidation to identify the reaction intermediate species formed during the oxidation mechanism. DRIFT spectra of the catalysts were collected by using a Frontier spectrometer device (PerkinElmer, USA). The spectrometer was equipped with a mercury cadmium telluride (MCT) detector and a Praying Mantis (Harrick, USA) cell.

2.7. Catalytic testing

The vapor–phase benzyl alcohol (BnOH) oxidation was performed in air over Ag/MnO_2NRs catalysts in a vertically aligned quartz tube reactor (height = 0.45 m, inner diameter = 10 mm). In a typical reaction, 0.07 g of catalyst in powder form was added to spherical alumina beads with 3 mm diameter in a tube containing quartz wool at a weight ratio of 1:5. Before the oxidation reaction, the catalyst was pre–treated and activated at 270 °C for 1 h with the ramp rate of 5 °C in atmospheric pressure in the presence of air. The preloaded catalyst bed was further activated and dried in air for about 30 min and heated up to reaction temperature of 260 °C. Next, the reaction was started by feeding benzyl alcohol (BnOH) into a preheating zone (260 °C), where vaporisation took place. Then, the vapourised BnOH was mixed with a stream of oxidant (air) and passed over the catalyst bed. A syringe pump was used in all the experiments to control the flow of 2 mL per hour flow rate of benzyl alcohol, and a cold trap (ice bath) used at the reactor outlet to collect the liquid by–products. A small sample of the liquid products from the reaction were collected in the reactor exit and quantitatively examined in a gas chromatography–mass spectrometer (GC–MS, Shimadzu 2014) fitted with an EB 5 column (30 m 0.25 mm 0.25 m). A mixture of BnOH in equal molar ratios was used to determine the sensitivity of the GC signal for the specific product. It is important to notice that the BnOH was not injected continuously instead in dropwise at regular intervals. The following equations were used to calculate the conversion, selectivity, and rate of BnOH oxidation to products at a specific temperature.

$$\text{conversion}\,(\%) = \frac{\text{moles of BnOH converted}}{\text{moles of BnOH feed}} \times 100$$

$$\text{selectivity}\,(\%) = \frac{\text{moles of product formed}}{\text{moles of BnOH converted}} \times 100$$

$$\text{rate} = \frac{FX}{W}$$

where F is the flow rate of BnOH (in moles), X is the fractional conversion of BnOH, and W is the weight of catalyst (in grams) [23].

Weight hourly space velocity (WHSV) is calculated based on the below formula:

$$\text{WHSV} = \frac{\text{Flow of BnOH feed}}{\text{Weight of the catalyst}}$$

Benzaldehyde (BnZA) yield (%) has been calculated through this formula.

$$\text{Yield}\,(\%) = \frac{\text{Selectivity of desired product X BnOH conversion}}{100}$$

2.7.1. Computational methods (DFT study)

We have modeled a MnO_2 surface using density functional theory techniques to get further insight into the experimental results using the Vienna Abinitio Simulation Package (VASP) [33,34]. The surface is created from the optimized bulk geometry of tetragonal MnO_2 (space group I4/M) along the (0 0 1) orientation. Infinite periodicity is assumed along X and Y directions and along the Z direction, vacuum region of 15 Angstrom is applied to create the surface slab. Benzyl alcohol molecule is adsorbed on the pristine surface as well as on the surface in presence of Ag adsorbate. The adsorption energies are calculated in each case to understand the effect of the Ag atom in the energetics. A Gamma centered K grid is used for the Brillouin zone integration and a plane wave kinetic energy cut off of 520 eV is used. Generalized gradient approximation (GGA) is used to account for the exchange and correlation interactions, in the Perdew–Burke–Ernzerhof (PBE) approximation [35]. The pseudo potentials used in the calculations were that of the Projected augmented wave (PAW) method [34,36].

3. Results and discussion

The schematic representation for the formation of Ag decorated MnO_2NRs is present in Scheme 1. The structure and morphology of MnO_2NRs were analysed systematically by using FE–SEM and reported in the supplementary information (Fig. S1). The existence of smooth and homogeneous nanorods of α–MnO_2 is clearly depicted in FE–SEM images Fig. S1(a–c). Further, to gain a deeper understanding of the structural data of the as–prepared α–MnO_2 nanomaterials, the microscopic TEM, HRTEM, and SAED analyses were also determined (Fig. 1). The TEM images of α–MnO_2NRs are shown in Fig. 1a, displaying the morphological feature that resembles a nanorod shaped particles. The microscopic depicted the homogenously distributed nanorods with a diameter of around ~ 25 nm and this can clearly be presented in Fig. 1 and Fig. S2. The measured lattice distances are about 0.49, 0.24, and 0.31 nm, which corresponds to the (2 0 0), (2 1 1), and (3 1 0) planes of α–MnO_2NRs, respectively, also measured angle between (2 0 0) and (2 1 1) plane is around 90° which can be seen from the HRTEM images (Fig. 1b) and Fig. S3 [28,29]. Multiple diffraction rings can be seen in Fig. 1c, which shows that the α–MnO_2 nanorods are highly crystalline and arranged in order. The (2 0 0), (2 2 0), (3 1 0), (4 0 0), (3 0 1), (4 1 1) and (4 3 1) planes correspond to α–MnO_2NRs and are clearly visible with diffraction rings, which are in good agreement with the XRD results (Fig. 3). It was confirmed that the α–MnO_2 with nanorods like structure was formed and it is also substantiated with the SEM, TEM, and HRTEM results. It can be concluded that the reaction of $KMnO_4$ and $MnSO_4{\cdot}H_2O$ led to the successful formation of α–MnO_2NRs structure. Additionally, one can conclude from histograms of particle size distribution by TEM images, the average diameter of ~ 25 nm and the average length of rods ranging between 300 nm and 1 μm (SI Fig. S2).

The R. Rajesh *et al.* modified the procedure in synthesising the precise average size and shape controlled spherical AgNPs (~6 nm) [21,31]. Dodecylamine and formaldehyde are the most important regents used in order to create uniformly distributed spherical silver nanoparticles, as can be seen from the TEM and HRTEM pictures in Fig. 2 (a, b). In general, it should be noted that a suitable reduction rate would be extremely advantageous in the synthesis of AgNPs with a confined size distribution. Generally, the nucleation process is speed up by the strong reducing agents (such as $NaBH_4$ or $LiBH_4$), thus, making it difficult to produce NPs with a uniform size [37]. It has been demonstrated in numerous investigations that the metallic NPs can be produced by using a weaker reductant, such as amine–borane complexes [38–40]. However, the weaker reducing agent fails in the synthesis of smaller AgNPs. The drawback of using external reducing agent either a stronger or weaker, thus, making it difficult to obtained mono–disperse with uniform metal nanoparticles due to the rapid reduction step during nucleation process. In this work, dodecylimine played a major role in the formation of AgNPs. Dodecylimine is formed by reducing dodecylamine with formaldehyde and the advantages of dodecylimine agent are many such as (i) it is acting as a reducing agent as well as encapsulating agent,

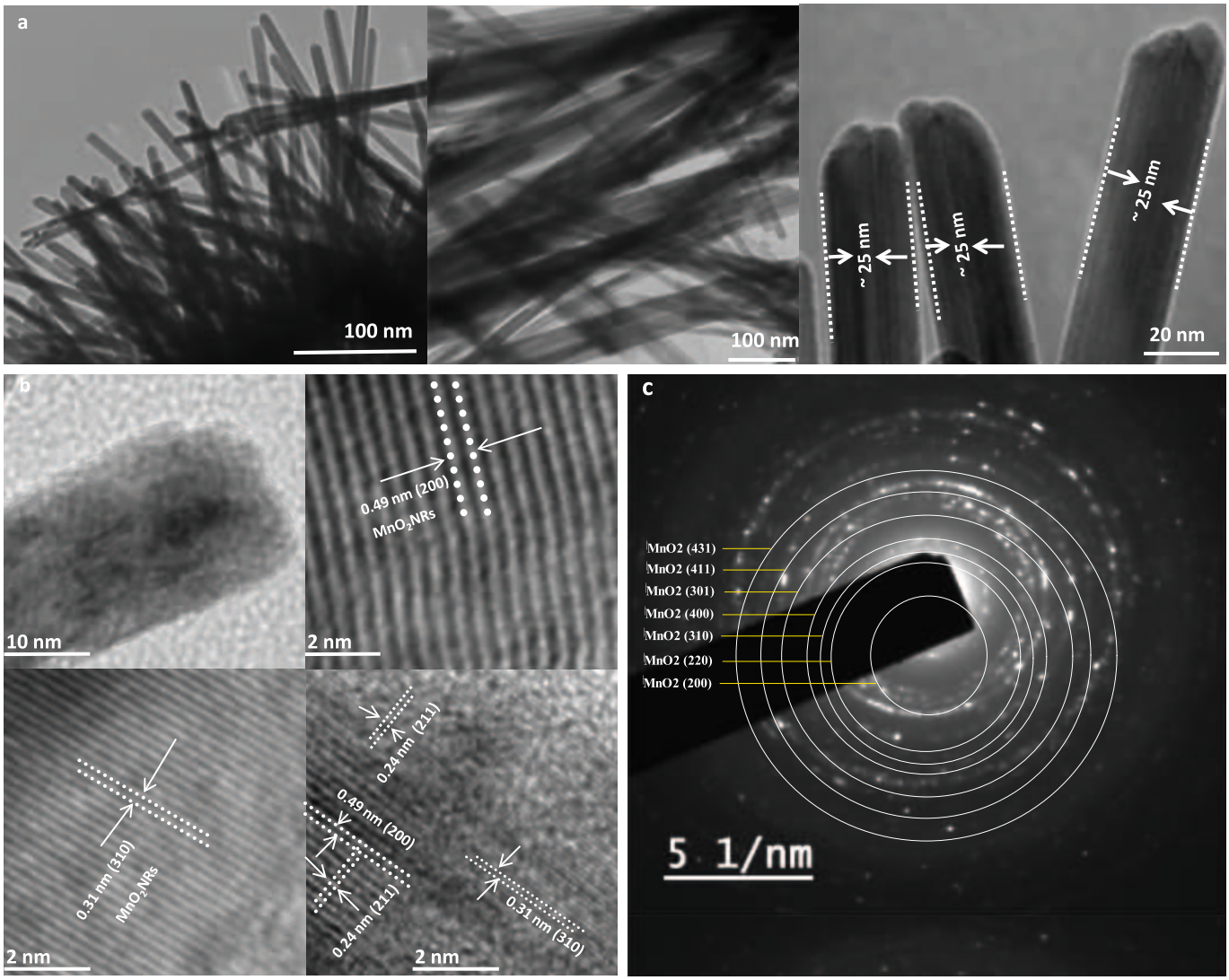

Fig. 1. The microscopic images (a–c) TEM, HRTEM and HRTEM–SAED patterns of α–MnO_2NRs.

(ii) imine part helps to reduce the ion Ag^+ to metallic state Ag^0 and the aliphatic long chain helps to stabilize and avoid the AgNPs aggregation and finally, resulted in the production of uniform monodisperse smaller AgNPs in room temperature. Multiple TEM images with different magnifications in various regions were analyzed for better understanding the surface morphology and the details of controlled uniform sizes of AgNPs. Fig. 2 depicts the (a) AgNPs with a perfect spherical morphology and homogeneous distributions. The size distribution histograms were presented by measuring the diameter of at least 500 particles for each sample to understand the physical size and the distribution from TEM images; it should be noted from the similar figure Fig. 2c, the majority of the particles possessed an average size of 6 nm. To validate these findings, we performed HRTEM analysis of synthesized AgNPs Fig. 2(b). HRTEM images displayed that each small particle formed a spherical morphology with no particle agglomeration. Furthermore, it is hard to find lattice fringes in the Ag spherical particles, indicating that the formed AgNPs may be amorphous in nature. However, some of Ag particles show metallic Ag lattice fringes at 0.23 nm in in–dept HRTEM images in Fig. S4. Moreover, the particle size is visible from HRTEM images and depicted that the AgNPs had an average size of 6 nm, confirming the size and homogeneity of the synthesized AgNPs. The extensive XPS analysis was applied to determine the chemical environment and Ag oxidation state of the AgNPs at the Ag 3d core levels. From XPS, there is a good agreement that the presence of metallic silver spectral values corresponding to the Ag $3d_{5/2}$ and Ag $3d_{3/2}$ core levels, the binding energies of AgNPs are 367.95 and 374.1 eV, respectively (Fig. 2d) [31,41]. UV–Vis absorbance spectroscopy further confirms that the metallic character of synthesised AgNPs based on the emergence of a surface plasmon resonance peak at 440 nm was appeared in Fig. 2e [41].

P–XRD analysis was used to determine the phase purity and crystallinity of the synthesised α–MnO_2NRs (Fig. 3 (a)). The synthesised α–MnO_2NRs P–XRD patterns displayed clearly defined diffraction peaks that are consistent with the crystalline phases of α–MnO_2NRs reported from JCPDS data (card no. 44–0141) [28]. The corresponding planes (1 1 0), (2 0 0), (3 1 0), (4 0 0), (5 1 0), (3 0 1), (5 2 1), (0 0 2), and (5 4 1) respectively, are represented by the diffraction peaks that are assigned to 12.8°, 8.16°, 28.9°, 36.67°, 41.9°, 49.9°, 60.32°, and 65.51°, 2θ angles respectively (Fig. 3) [29]. While there is no significant diffraction peak of an impurity was found, confirming that the purity of the phase, the sharp and intense peaks correspond to the presence of α–MnO_2NRs in a highly crystalline form. Using P–XRD patterns and the Debye-Scherrer equation, it was determined that the average crystallite size of α–MnO_2NRs was around ~ 25 nm. There are no Ag phases detected in XRD patterns after the incorporation of AgNPs in α–MnO_2NRs with different loadings (Fig. S5). Interestingly, when we analysed thoroughly in Fig. S5, there are no XRD peak position changes after the Ag loadings. This indicates the Ag is located over the intrinsic α–MnO_2NRs surface and not in the inner lattice or the bulk.

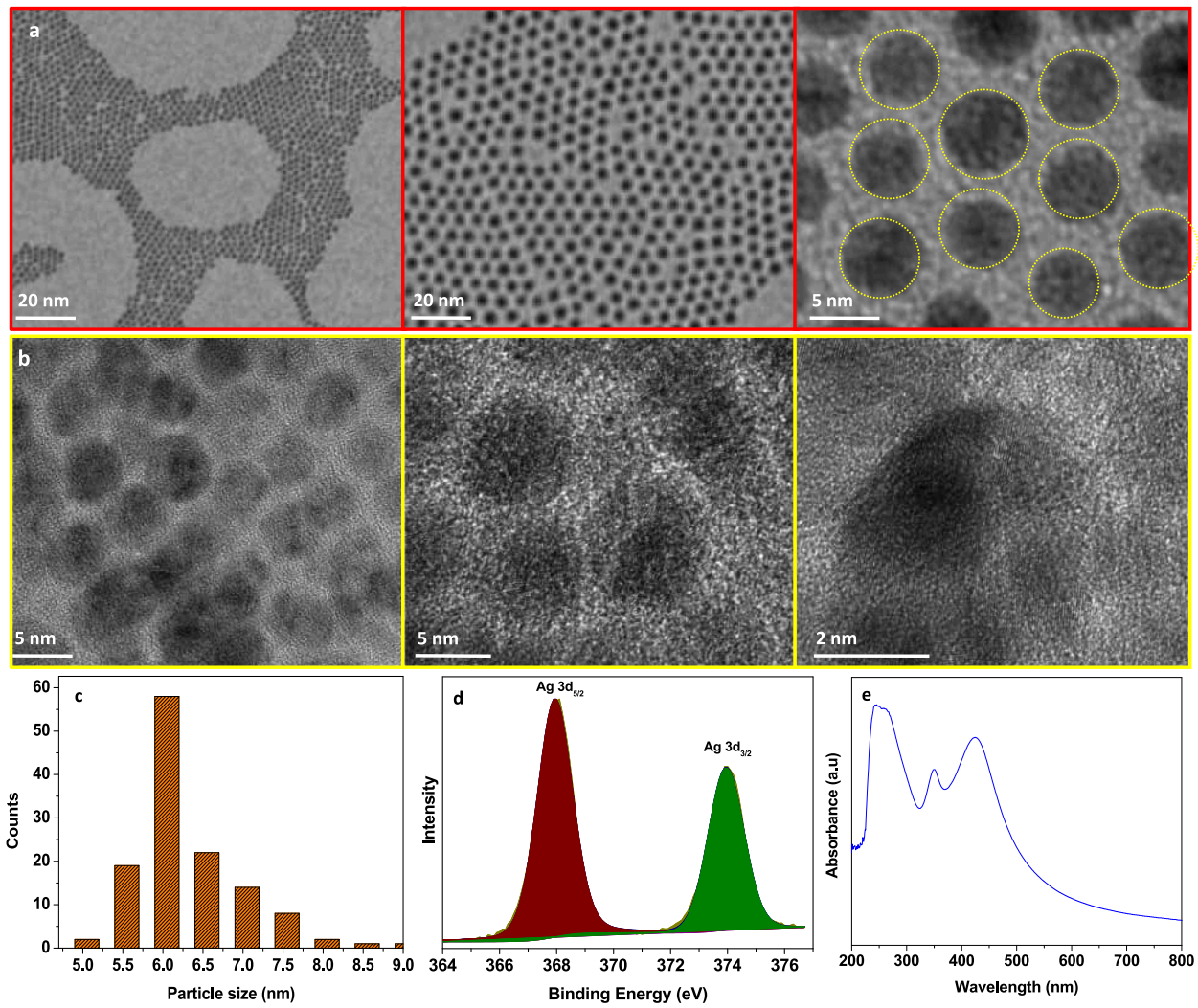

Fig. 2. (a, b) TEM and HRTEM images of AgNPs in various magnifications, (c) Particles size distribution of AgNPs, (d) XPS analysis of Ag 3d scan of AgNPs and (e) represents UV–Visible absorbance spectra of self–assembled AgNPs.

For additional phase confirmation, the FT–Raman spectrum for α–MnO_2NRs and 1Ag/α–MnO_2NRs has been analyzed and it is presented in Fig. 3(b) and Fig. S6. A low wavenumber peak at 181 cm^{-1} is appeared for both samples, and it can be attributed to an external mode that was originated from the translational motion of [MnO_6] molecules [42]. Additionally, the Raman spectra of α–MnO_2NRs and 1Ag/α–MnO_2NRs presented two distinct peaks that are typical for α–MnO_2 *i.e.,* one at 639 cm^{-1} due to the Mn–O symmetric stretching modes and another at 571 cm^{-1} due to the deformation modes of the Mn–O–Mn chain in MnO_2 molecule [43,44]. These results substantiated the XRD results and concluded that the MnO_2 nanorods are in pure form of tetragonal phase. However, interesting results were found over 1Ag/α–MnO_2NRs catalyst, as shown in Fig. 3(b), where the strength of the Mn–O symmetric stretching mode was considerably reduced, and the peaks appearance was shifted to 634 cm^{-1} (see Fig. S6) [42]. It must be due to the strong electrostatic interactions between lattice oxygen in α–MnO_2NRs and AgNPs.

As shown in Fig. 3 (c, d) and Fig. S7, an XPS study was carried out to examine the chemical state of Mn, O, and Ag elements in α–MnO_2NRs and 1Ag/α–MnO_2NRs materials. The Mn and O elemental signals are visible in the pure α–MnO_2NRs XPS spectrum. In addition, Mn 2p and O 1 s peaks indicate the presence of manganese oxide species. A spin–orbit doublet of Mn $2p_{1/2}$ and Mn $2p_{3/2}$ are presented in the Mn 2p area depicted in Fig. 3(c) and are positioned at binding energies of 654.20 and 642.40 eV, respectively [29,30,42,45]. Whereas, MnO_2 was formed, as evidenced by the 11.8 eV spin–energy separation [26]. Additionally, it has been reported that the binding energies of the Mn $2p_{3/2}$ electron for the Mn^{4+} and Mn^{3+} states are assigned to 644.06 and 642.40 eV, further confirming the final chemical composition as MnO_2 [30]. Interestingly, the Mn^{4+} XPS peak intensity is significantly reduced in the 1Ag/α–MnO_2NRs sample. It was also observed that the peak positions for $Mn2p_{3/2}$ and $Mn2p_{1/2}$ were displaced into 642.25 and 653.85 eV B. Es, respectively. After AgNPs loading, the Mn^{3+} peak ($Mn2p_{3/2}$) is noticeably shifted with enhanced intensity and appeared at 642.25 eV spectrum. Additionally, the gap between $Mn2p_{3/2}$ and $Mn2p_{1/2}$ is reduced (from 11.8 to 11.6). This indicates that the AgNPs anchored on the α–MnO_2NRs with strong electrostatic interactions [42]. In the case of O 1 s spectra (Fig. 3d) of α–MnO_2NRsis composed of two oxygen–containing chemical bonds, namely surface adsorbed oxygen atoms (O_{ads}.), and lattice oxygen from Mn–O–Mn bonds (O_L) [45]. One of the strong peaks from Mn–O–Mn bonds (O_L) at 529.8 eV, and the weak peaks were of surface adsorbed oxygen bonds (O_{ads}.), which had a centered at 531.5 eV. The O_L (*i.e.,* O atoms originating from Mn–O–Mn lattice) intensity of XPS peak significantly decreased and peak shifted to 529.9 eV after incorporation of AgNPs on α–MnO_2NRs due to the cyclic formation of oxygen vacancies and lattice occupancy of atomic O_{ads}. Additionally, the significant shift is evident probably due to the adsorbed oxygen peak intensity increased at 531.5 eV and this resulted in the

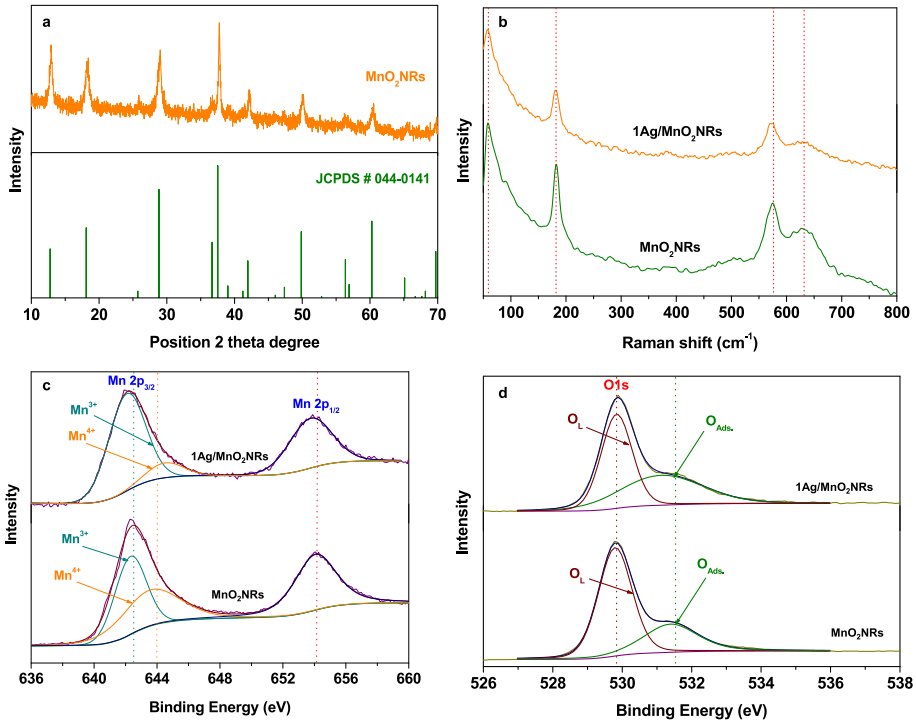

Fig. 3. (a) P–XRD of α–MnO_2NRs, (b) Raman spectrum of α–MnO_2NRs and 1Ag/α–MnO_2NRs catalysts and (c, d) curve–fitted Mn 2p and O1s core–level spectrum of α–MnO_2NRs and 1Ag/α–MnO_2NRs respectively.

generation of increased oxygen vacancies in the α–MnO_2NRs support system [45]. The XPS analysis was used to determine the Ag oxidation state of the 1Ag/α–MnO_2NRs nanocatalyst Fig. S7. The Ag $3d_{5/2}$ and Ag $3d_{3/2}$ core level binding energies appeared without any considerable shift (367.95 and 374.1 eV) similar to bare AgNPs (Fig. 2e), thus, it confirms and are in good agreement with that of metallic silver values [46]. Table S1 summarizes the apparent XPS binding energy values of MnO_2NRs and 1Ag/MnO_2NRs catalysts.

The corresponding HRTEM images and its elemental mapping of the as–prepared 1Ag/α–MnO_2NRs sample are shown in Fig. 4(a–c). HRTEM images displayed spherical shaped silver nanoparticles distributed on α–MnO_2NRs surface. Further to understand the Ag deposition on α–MnO_2NRs, the elemental composition was systematically analysed by the HRTEM–EDS mapping and was monitored by using energy dispersive X–ray (EDX) nanoanalysis as shown in Fig. 4(a). The images clearly indicate the presence of Mn, O, and Ag elements on the 1Ag/α–MnO_2NRs nanocatalyst. Further, the morphology and interface between Ag and α–MnO_2NRs of the prepared catalyst (1Ag/α–MnO_2NRs) was studied by analyzing the HRTEM results as presented in Fig. 4(b, c). The HRTEM images revealed the size and shape morphology of the α–MnO_2NRs are intact and retained even after AgNPs deposition. The measured diameter of the α–MnO_2NRs from HRTEM is ~ 25 nm in size, this value was well matched before Ag loadings. Moreover, ultra–fine nanosized AgNPs were highly dispersed on the α–MnO_2NRs, and the size distribution ranges from 6 to 7 nm with majority of AgNPs had mean size of 6.5 nm. The strong metal (Ag)/metal oxide (α–MnO_2NRs) interfaces were analysed and determined by higher magnifications (Fig. 4c). It is highly visible from Fig. 4(c) that the mixed lattice fringes of Ag and α–MnO_2NRs exhibited *i.e.,* Ag fringes of 0.231 nm corresponds to (1 1 1) plane and α–MnO_2NRs fringes of 0.31 nm and 0.24 nm corresponds to (3 1 0) and (2 1 1) lattice planes of α–MnO_2NRs, respectively. Moreover, this can be clearly concluded and substantiated by deep analysis of HRTEM images in the similar fashion (Fig. 4c) between AgNPs and α–MnO_2NRs support. Moreover, it is shown the presence of atomic sharing between AgNPs and the support matrix of α–MnO_2NRs, which enables the strong metal support interactions. Further, the amorphous parts of silver nanoparticles over the α–MnO_2NRs were depicted in Fig. 4b. The advantages of amorphous silver nanoparticles are that they can bind strongly over the MnO_2NRs surface through the strong interfaces between Ag and α–MnO_2NRs surface.

The FT–IR analysis from Fig. 5a clearly represents the formation of α–MnO_2 nanorods. The Mn–O vibrations of octahedral MnO_6 in α–MnO_2NRs are denoted for the bands at about 719.9, 528.6, and 470.3 cm^{-1} wavenumbers including that are below 750 cm^{-1} [28,47]. The FT–IR spectral analysis is ascribed to the highly structural symmetry of α–MnO_2NRs. The absence of C–C, C = N, C–H, CH_2 and NH_2 stretching and bending vibrations clearly indicates that the encapsulating agent (dodecylamine) was completely decomposed or removed during calcination step. Moreover, the absence of 538 cm^{-1} peak indicates the Ag does not get oxidized and it retained the metallic nature after 350 °C for 5 h calcination. The Mn–O stretching and bending vibrations of α–MnO_2NRs considerably shifted to lower wave numbers region, which indicates the stronger metal–support interactions exhibited after the addition of AgNPs, thus, resulting the weakening of the Mn–O–Mn bond strength. The 1Ag/MnO_2NRs sample shows a higher lower shift values than the 0.5Ag/MnO_2NRs sample. Further increasing the Ag content (*i.e.*, 1.5 wt%), there is no peak shift was evident in the Mn–O vibrations mode, thus indicating the metal dispersion saturation occur at this stage.

The N_2 adsorption/desorption technique was used to characterize the pore architectures of the synthesised materials; the sorption isotherms, pore size distributions, and textural features are listed in Table 1. All samples exhibited a type–IV N_2 isotherm with H_2 hysteresis loop (Fig. 5b). Additionally, the pore size distribution in Table 2 showed that they were primarily distributed in the range of 4–6 nm and that the pore sizes calculated from the adsorption isotherms [48]. The introduction of Ag decreased the pore size, possibly due to the portion of Ag species covering the surface of MnO_2. The BET surface areas of the Ag loaded α–MnO_2NRs samples were slightly smaller than those of MnO_2NRs (41.5 $m^2.g^{-1}$) (as shown in Table 1). The percentage of Ag content was calculated with ICP–MS instruments that are presented in Table 1.

The H_2–TPR analysis was used to gain insights on the creation of

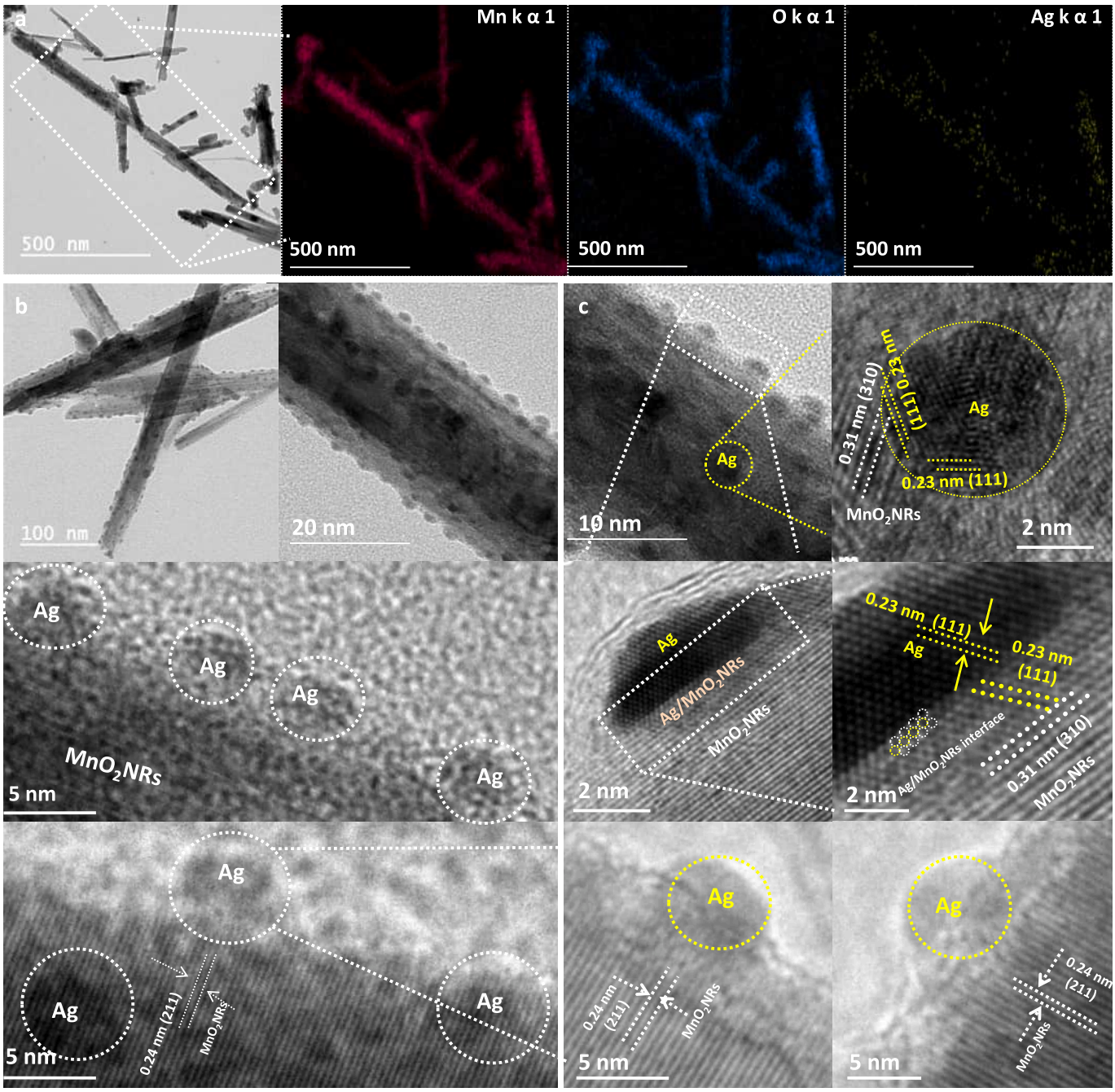

Fig. 4. (a–c) HRTEM images of 1Ag/α–MnO_2NRs catalyst in different magnifications.

oxygen vacancies and the metal–support interactions on the Ag loaded MnO_2NRs (Fig. 6a). The TPR profile of MnO_2NRs sample analysed and reduction profile had broad peaks between 250 and 550 °C, which was divided into two peaks, the peaks are designated as α and β peaks, respectively. Additionally, at higher temperatures, a peak at 680 °C was observed and this denoted as γ–peak. These three peaks *i.e.,* below 400 °C (α–peak), 400–475 °C (β–peak), and above 650 °C (γ–peak), might be assigned to the sequential reduction of MnO_2 → Mn_2O_3 → Mn_3O_4 → MnO respectively [45,46]. Following the addition of silver, all reduction peaks are shifted noticeably toward low temperature region, thus, improving the reducibility of MnO_2, which was consistent with previous reports [47]. Additionally, the observed β peak was seen more intense and sharper. Henceforth, all these findings demonstrated the higher surface oxygen species availability over 1Ag/α–MnO_2NRs catalysts and further, the reduction of MnO_2 to low valence manganese species which was increased by the hydrogen spill-over effect by silver atoms to manganese oxides, which is in line with the O 1 s XPS spectra result.

O_2–TPD was used to investigate the surface oxygen species of all catalysts, and the comparative results are shown in Fig. 6b. As can be seen in Fig. 6b, the molecular oxygen species that has been adsorbed on oxygen vacancies and the surface labile oxygen, and the crystal lattice oxygen are responsible for the desorption peaks that occur at temperatures around 200 °C, 450 °C, and 590 °C, respectively. Interesting results were observed after loading AgNPs on the α–MnO_2NRs, the crystal lattice of the oxygen desorption peak shifted to higher temperature range for the 0.5 and 1 wt% Ag loaded samples. These phenomena were typically reflecting the enhancement of oxygen vacancies to provide the higher cyclic O_2 adsorption capacity during the catalytic oxidation and henceforth, the stronger interactions between Ag and adjacent lattice O

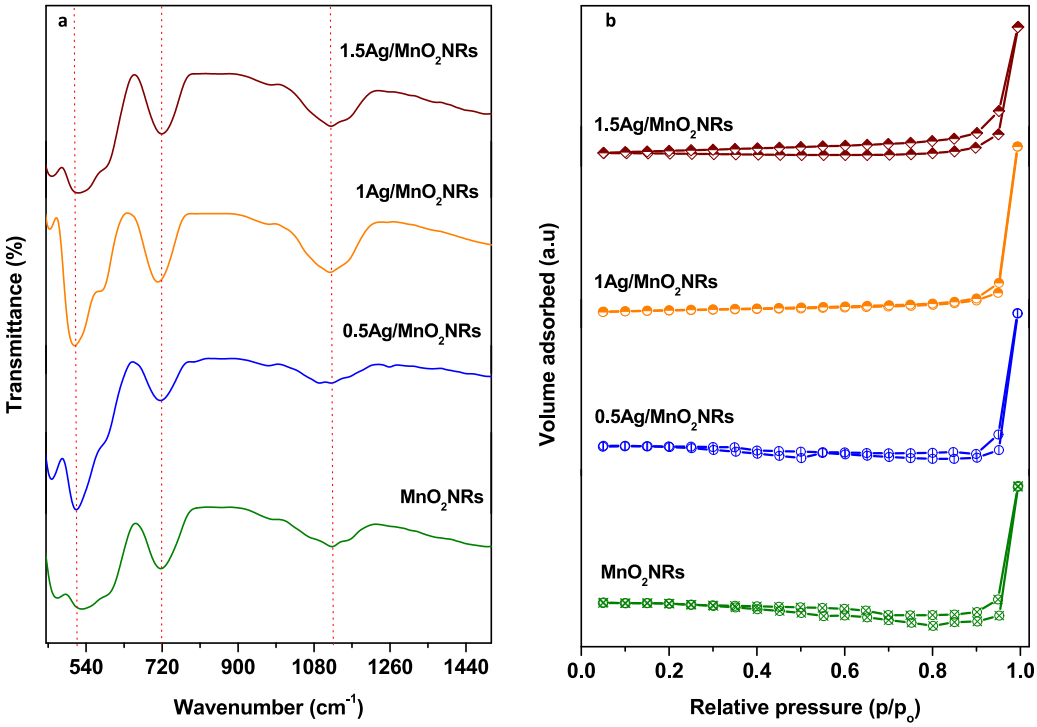

Fig. 5. (a) FT–IR and (b) BET physisorption isotherms of various AgNPs loaded on α–MnO_2NRs catalysts and bare MnO_2NRs support.

Table 1
Textural properties and metal composition of as–prepared catalysts.

Sample	S_{BET}[a] ($m^2.g^{-1}$)	D[b] (nm)	V^c_{pore} ($cm^3.g^{-1}$)	Ag content (wt.%)[d]
α–MnO_2NRs	42.5	5.6	0.55	n.d.
0.5Ag/α–MnO_2NRs	41.1	5.4	0.44	0.501
1.0Ag/α–MnO_2NRs	40.6	5.0	0.57	1.02
1.5Ag/α–MnO_2NRs	38.2	4.1	0.47	1.501

[a] Specific surface area obtained by BET. [b]BJH pore diameter calculated from the adsorption branch. [c]Estimated total pore volume. [d]Elemental molar ratio of the samples detected by ICP–MS.

atoms in MnO_2 structures was evident [45,47]. Further at higher loadings *i.e.,* 1.5 wt% Ag, the O_2-desorption peak shifted to lower temperature region. It is indicating that the AgNPs dispersion attained saturation state on the MnO_2NRs.

3.1. Application in selective oxidation of BnOH using MnO_2NRs and AgNPs/MnO_2NRs

The oxidation of benzyl alcohol (BnOH) was performed at light–off temperatures as shown in Fig. 7(a, b) to evaluate the reaction kinetic parameters of the as–synthesised α-MnO_2NRs and Ag/α–MnO_2NRs catalysts [23,24,28,48]. In order to acquire kinetically controlled data, a catalyst amount of 0.07 g was tested in the activity runs. The catalyst screening studied the effect of reaction temperature between 200 and 280 °C (Fig. 7a). The Activation energy (E_a) and the activation parameters, such as the enthalpy of activation ($\Delta H^{\#}$) and entropy of activation ($\Delta S^{\#}$) has been calculated with varying the temperature between 200 and 260 °C with 0.07 g catalysts and with a feed rate of 2 mL/h (Fig. 7b and Fig. S8) using Eqs. (1) & (2). At elevated temperatures, the apparent BnOH conversion rate was estimated.

In Fig. 7a, the apparent rate constant values for the MnO_2NRs and 1Ag/α–MnO_2NRs catalysts at various temperatures are shown. As we know, the faster molecular motion and higher chance of collisions in bond scissions initiate the higher reaction rate constant and typically, the activity is linearly dependent with temperature and reached saturation point (200 – 260 °C).

Table 2
State of the art catalysts reported in the literature for vapor phase oxidation of BnOH and comparison with the present work.

[a]Catalyst	Yield (%)	Temp. (°C)	Oxidant O_2/Air	[b]WHSV (h^{-1})	[c]Rate (mol $g^{-1}h^{-1}$)	Ref.
α-MnO_2NRs	38	260	Air	28.5	0.1043	This work
1Ag/ α–MnO_2NRs	98	260	Air	28.5	0.2719	This work
1Ag(C)/ α–MnO_2NRs	64	260	Air	28.5	0.1774	This work
Ag–HMS	96	310	O_2	12	0.1021	[13]
Nano–Au	61	240	O_2	15	0.0811	[14]
K–Cu–TiO_2	99	203	O_2	0.8	0.0084	[15]
Ag/Ni–fiber	84	380	O_2	25	0.1529	[16]
Ca − Ag/SiO_2	67	240	O_2	6.5	0.0386	[17]
Co/NaY	45	350	O_2	6.5	0.026	[18]
Ag/SiO_2	84	350	O_2	6.5	0.048	[19]
Au/TiO_2	80	320	O_2	2.84	0.0201	[20]
$Cu_{0.25}Mn_{2.75}O_4$	82.6	300	O_2	10	0.0736	[22]
$Co_{0.25}Mn_{2.75}O_4$	69.2	300	O_2	10	0.0613	[22]
α-MnO_2	27	250	Air	20	0.0478	[23]
α-MnO_2/CeO_2	28	250	Air	20	0.049	[23]
1% Au − Cu/ SiO_2	98	260	Air	6.5	0.056	[24]
Cu − Na–ZSM–5	80	400	O_2	2.6	0.0051	[49]

[a] Reaction conditions: 0.07 g of catalyst, 260 °C and 25 mL.min^{-1} (air). [b]WHSV were calculated by feed flow divided by weigh of the catalysts. [c] $rate = \frac{FY}{W}$ where F is the flow rate of BnOH (in moles), Y is the fractional yield of benzaldehyde, and W is the weight of catalyst (in grams).

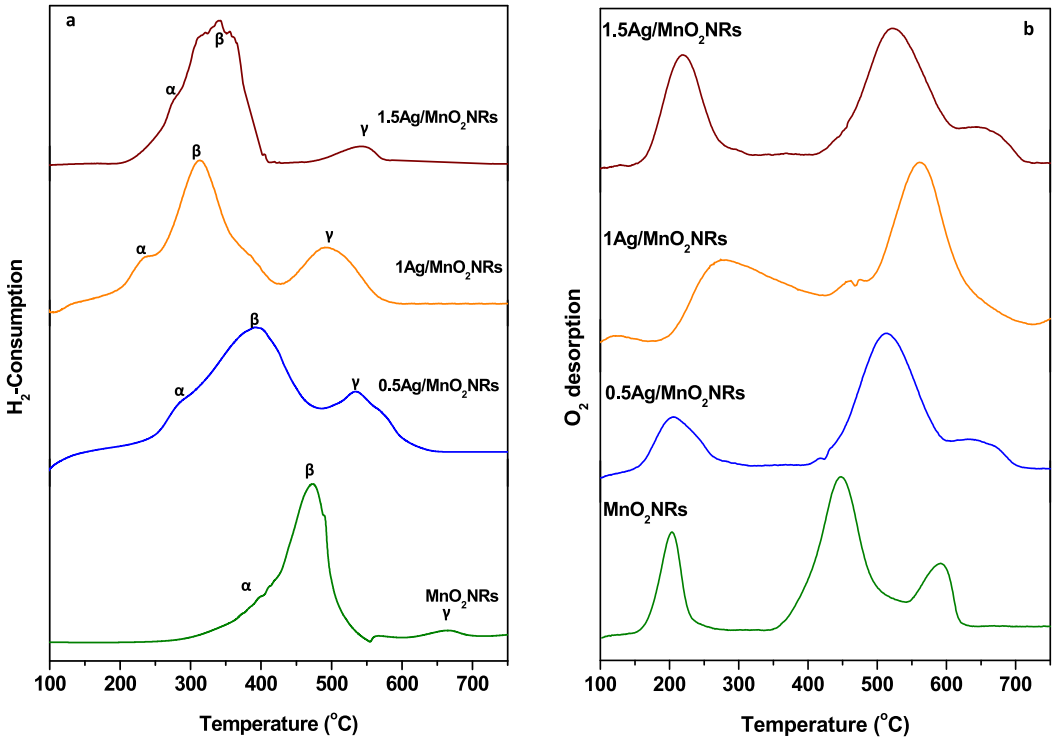

Fig. 6. Temperature programmed analysis. (a) H_2–TPR and (b) O_2–TPD profiles of different AgNPs loaded α–MnO_2NRs catalysts.

$$\ln K = -\frac{Ea}{R}\frac{1}{T} + \ln A \quad (1)$$

where E_a is the activation energy, R is the universal gas constant, and A is the pre-exponential factor. We calculated the activation energy for the oxidation process from the apparent rate constants at various temperatures (Fig. 7b). For the catalysts α–MnO_2NRs and various Ag loaded α–MnO_2NRs, we calculated a linear relationship between ln $k_{BnOH\ conversion}$ (mol $g^{-1}h^{-1}$) and the reciprocal of temperature from which we estimated the activation energy of this reaction. In Table S4, the activation energies (E_a) for the catalytic oxidation of BnOH over nanocatalysts of α–MnO_2NRs and various Ag loaded α–MnO_2NRs were measured and are listed. Notably, the measured E_a values for the 1Ag/α–MnO_2NRs catalyst are significantly greater than the MnO_2NRs catalyst support. Thus, confirms that the activation energy primarily depends on silver nanoparticles [47]. Thus, it is evident that the performance of the reaction is significantly influenced by the properties of the AgNPs [19]. Additionally, the Eyring equation (eq (2) is used to determine the activation parameters such as the enthalpy of activation (ΔH#) and entropy of activation (ΔS#):

$$\ln\left(\frac{K}{T}\right) = \ln\left(\frac{KB}{h}\right) + \frac{\Delta S\#}{R} - \frac{\Delta H\#}{R}\left(\frac{1}{T}\right) \quad (2)$$

The Table S4 implies the thermodynamic constraints for activation energy barrier Ea, enthalpy ΔH# and entropy ΔS# activation at elevated temperatures. 1Ag/α–MnO_2NRs have the least positive ΔH# values, whereas MnO_2NRs have the highest positive ΔH# values. Furthermore, the ΔS# is the least negative value for MnO_2NRs and the highest negative value for 1Ag/α–MnO_2NRs. Fig. S9 shows a comparison of the apparent rate constants for the various Ag loaded α–MnO_2NRs and MnO_2NRs nanocatalysts, with the $k_{BnOH\ conversion}$ (mol $g^{-1}h^{-1}$) values follows the order: 1Ag/α–MnO_2NRs > 1.5Ag/α–MnO_2NRs > 0.5Ag/α–MnO_2NRs > α–MnO_2NRs. The outcome of rate constant dependency and correlation with temperature was clearly presented and the 1Ag/α–MnO_2NRs is a more efficient catalyst than MnO_2NRs. As a result, it can be concluded that MnO_2NRs decorated with Ag nanoparticles perform better in terms of catalytic properties and performance when used in the BnOH oxidation reaction.

The influence of catalyst amount of MnO_2NRs and 1Ag/α–MnO_2NRs on the BnOH oxidation reaction has been investigated in order to determine the optimal reaction parameters, and the results are shown in Fig. 7(c) (at constant reaction temperature 260 °C). We found as the catalyst amount increased, the BnOH conversion increased gradually and reached maximum activity at 0.16 g for the MnO_2NRs catalyst and 0.07 g for the 1Ag/α–MnO_2NRs catalyst, respectively. Interestingly there is no change in the benzaldehyde selectivity for both catalysts (MnO_2NRs shows ~ 99 % and 1Ag/α–MnO_2NRs is ~ 98%). Similarly, the effect of flow rate has been carried out by changing BnOH feed rate with constant catalyst amount of 0.07 g at 260 °C. Maximum catalytic activity obtained at 0.5 to 2 mL BnOH feed flow, further increasing the BnOH feed flow, the catalytic activity decreases (see Fig. S10). Finally, the reaction and catalyst parameters are optimised, thus, all experiments were carried out with optimal catalyst amount of 0.07 g, temperature 260 °C and 2 mL h^{-1} feed flow rate. Fig. 7(a) shows the BnOH conversion and selectivity (steady data after 1 h) toward products such as benzaldehyde, dibenzyl ether, benzoic acid, and benzyl benzoate over different catalyst compositions of MnO_2NRs and 1Ag/α–MnO_2NRs [19]. As expected, no reaction is seen to occur when the blank test run was tested. Over 1Ag/α–MnO_2NRscatalyst, exhibited very high activity and reaching close to ~ 99% conversion with ~ 98% benzaldehyde selectivity. Over pure MnO_2NRs catalyst support exhibited relatively lower activity compared to AgNPs supported catalysts and achieved 38% conversion and 99% benzaldehyde selectivity. This implies that the AgNPs catalysts are primarily responsible for the superior performance in the oxidation activity. Further, maximum conversion value of 99% obtained, thus almost complete BnOH was transformed to benzaldehyde upon addition of 1 wt% Ag loaded MnO_2NRs catalyst. Further increase AgNPs from 1 to 1.5 & 2 wt% content, the activity significantly declined *i.e.*, conversions 75% (1.5Ag/MnO_2NRs) and 58% (2Ag/MnO_2NRs). However, selectivity toward benzaldehyde is slightly reduced among all Ag loaded α–MnO_2NRs catalysts compared to pure MnO_2. While MnO_2 also exhibited the highest selectivity of ~ 99% toward benzaldehyde,

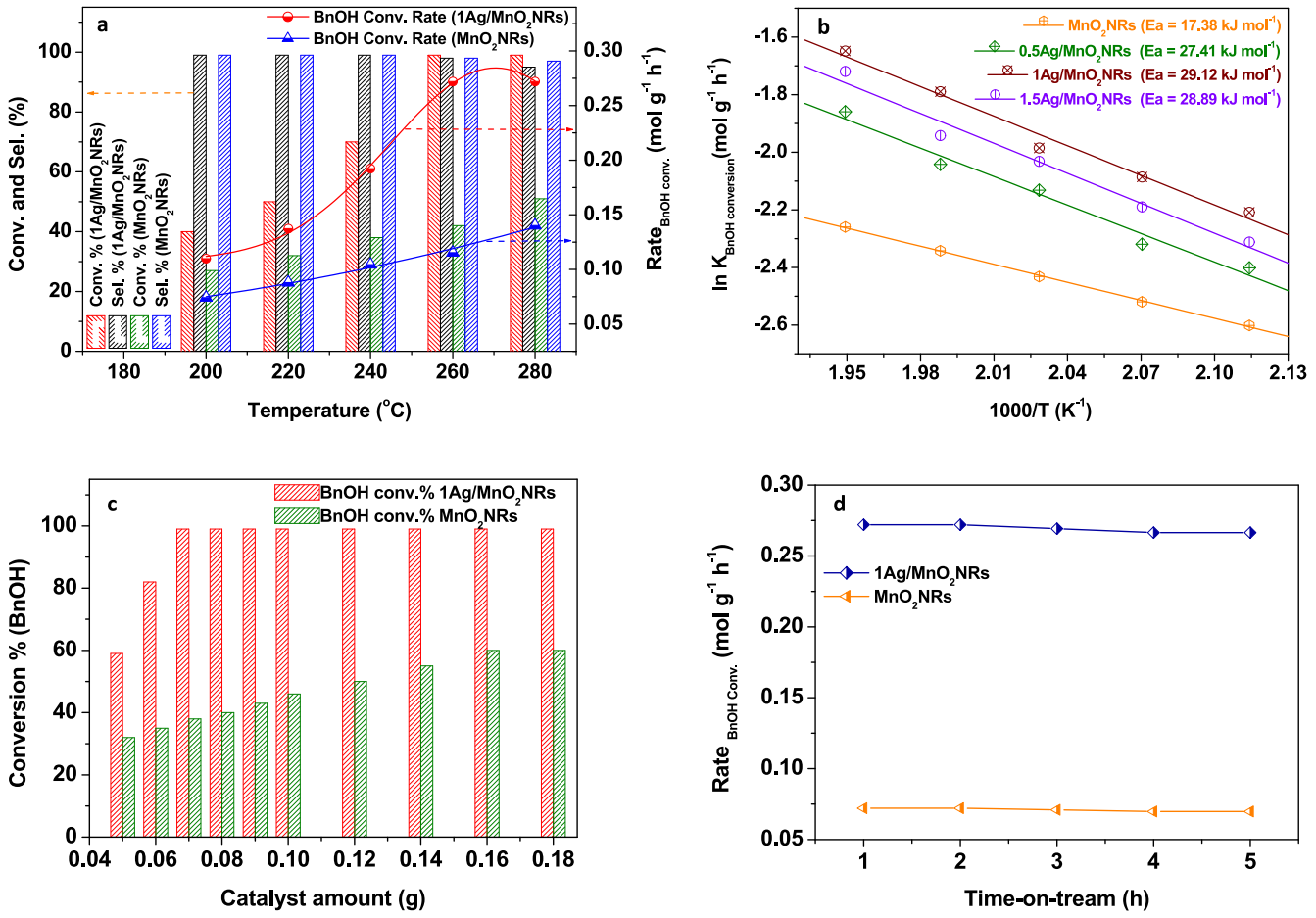

Fig. 7. BnOH oxidation in various conditions: (a) selectivity, conversion, and rate of BnOH (conversion) at different temperatures (Feed 2 mL h^{-1}, catalysts amount 0.07 g) for the α–MnO_2NRs and 1Ag/α–MnO_2NRs. (b) Arrhenius plot between ln $k_{BnOH\ conversion}$ (mol $g^{-1}h^{-1}$) vs 1/T (k^{-1}) to calculate the activation energy (Feed 2 mL/h, catalysts amount 0.07 g) for various Ag loaded MnO_2NRs. (c) Effect of catalysts amount (Feed 2 mL/h, catalysts amount varied from 0.05 g to 0.18 g). (d) Effect of time–on–stream on the BnOH oxidation (Feed 2 mL/h, catalysts amount 0.07 g).

AgNPs containing compositions exhibited slight drop in selectivity between 98 and 99% (see Fig. 7a). Fig. 7d shows the stability of the 1Ag/α–MnO_2NRs and MnO_2NRs catalyst at various compositions over time–on-stream (TOS) for 5 h. It proves that neither the pure MnO_2 nor the 1Ag/α–MnO_2NRs catalysts not significantly deactivates after 5 h of TOS. These stability tests indicate that the AgNPs are contributed the enhanced reaction rate in BnOH oxidation compared to MnO_2 component. Further, the stability of the catalyst confirmed by the analysing spent catalyst by P–XRD, XPS and ICP–MS analysis. It is hard to find differences in P–XRD patterns of 1Ag/MnO_2NRs before and after BnOH oxidation (Fig. S11). It is indicating there are no significant changes in the crystalline structure of 1Ag/MnO_2NRs even after catalytic oxidation. Further, the valence state of Ag, Mn and O elements presents in the 1Ag/MnO_2NRs catalyst after reaction was confirmed by XPS analysis of Ag3d, Mn2p and O1s spectra (Fig. S12). Interestingly, one can clearly notice in Fig. S12, there is no differences in the XPS spectrum of Mn, O and Ag elements peak position. Indicated no valence changes occur on 1Ag/MnO_2NRs catalysts before and after catalytic reaction. In order to find out the silver leaching we applied 1Ag/MnO_2NRs catalyst for the ICP–MS analysis, we found the content of the Ag weight percent presents in the 1Ag/MnO_2NRs catalyst is 1.01, indicated there is no Ag leaching occurs during the BnOH oxidation reaction. The spent catalyst characterisation results clearly indicate the optimised 1Ag/MnO_2NRs catalyst has good stability even after catalytic oxidation.

3.2. Comparison with the benchmark catalysts

Different metal/MO_x catalysts reported in the literature have been compared in terms of rate of BnOH conversion, WHSVs and yield (BnZA) with that of present studied catalysts (see Table 2 and Fig. 8). The summary of the catalysts studied the benzyl alcohol is oxidised in the vapour phase over both noble and non-noble metals based catalytic systems. This is feasible with high BnZA yield at temperatures ranging approximately from the boiling point of benzyl alcohol (205 °C) to higher temperatures (as high as 400 °C). In most of the studies, BnOH conversions over reported catalysts are in the range of 58 to 100%, while BnZA selectivities reported between 95 and 100% range [48].

In comparison to high substrate (BnOH) conversion, the required product selectivity is significant from the perspectives of atom economy and to achieve green chemistry principles. Fig. 8 clearly shows the present work catalysts exhibited highest conversion rate at higher WHSVs when compared to all reported noble and non–noble metal supported metal oxide catalysts. The significant results were achieved at space velocity compared to the state of art catalysts tested conditions. In case Ag based catalysts such as Ag/HMS [13], Ag/Ni–Fiber [16] and Ag/SiO_2 [17,19] catalysts exhibited higher BnZA yield (*i.e.,* >84%), however it requires higher temperatures (above 300 °C) and also suffers from higher WHSVs and poor rate of the reaction. Similarly among all Au based catalysts, over Au-Cu/SiO_2 [24] achieved highest ~ 98% BnZA yield with 260 °C lower temperatures however it is suffers from the WHSV and low reaction rate. In another study, non–noble metal based catalysts such as Co/NaY [18], Cu Na–ZSM–5 [49], $Co_{0.25}Mn_{2.75}O_4$ [22]

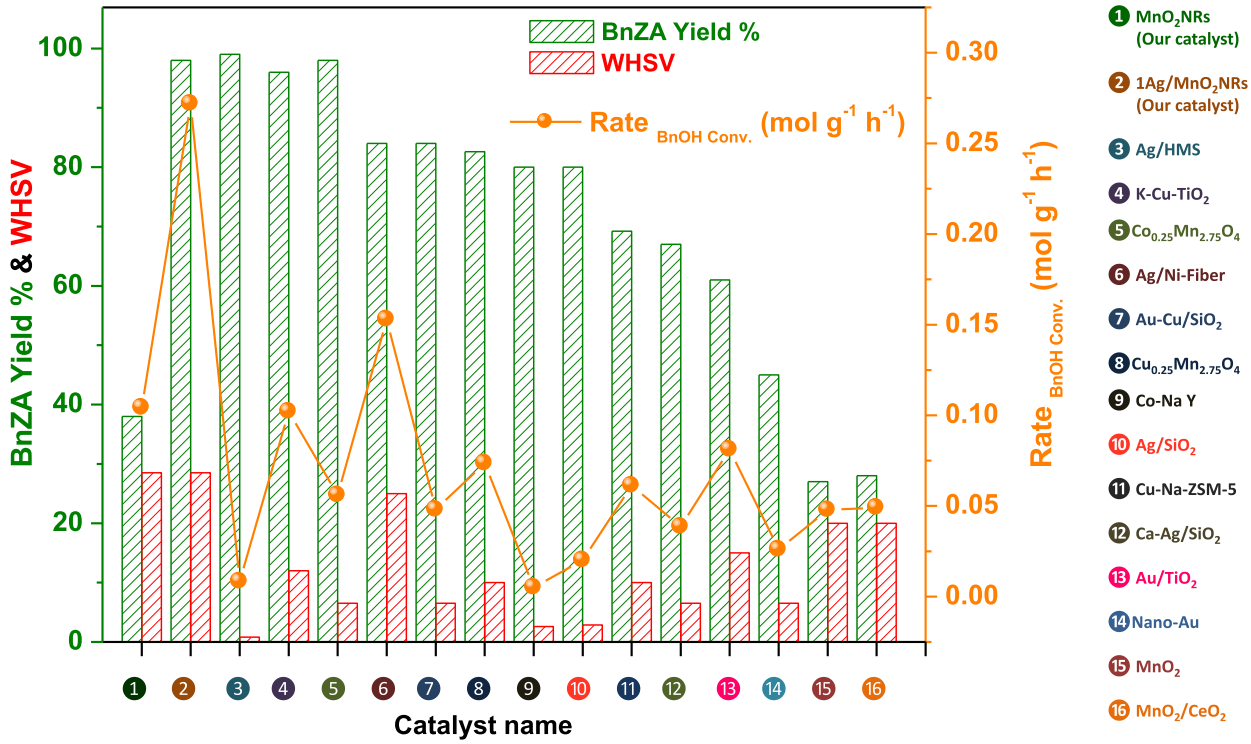

Fig. 8. Comparison of the most active catalysts reported in BnOH oxidation from the literature with the present work in terms of benzaldehyde yield and rate at different WHSVs.

and $Cu_{0.25}Mn_{2.75}O_4$ [22] catalysts were used in BnOH partial oxidation reactions, however, these catalyst required higher reaction temperatures (300–400 °C). Nevertheless, BnOH oxidation can be tested just above the boiling point of BnOH (205 °C), that has been reported by Jie Fan *et al.* and in his study, they achieved ~ 99% BnZA yield over K doped Cu–TiO_2 catalyst [15]. However, it shows at low WHSV 0.8 g h^{-1} with poor reaction rate (0.0084 mol $g^{-1}h^{-1}$). As a result, the current MnO_2NRs and AgNPs/MnO_2NRs catalysts shown higher activity compared to the catalysts discussed above and ones reported in the literature. Further, we compared the catalytic activity of this work (*i.e.*, 1Ag/MnO_2NRs) with conventionally reduced AgNPs loaded catalyst (1Ag(C)/MnO_2NRs). Profoundly the over 1Ag/MnO_2NRs catalyst achieved 1.532 times higher reaction rate than the conventionally reduced method (1Ag(C)/MnO_2NRs). The low activity is due to the randomly distributed big size AgNPs over MnO_2NRs (Fig. S13).

The catalysts have been thoroughly characterised in order to understand the structure, surface chemistry, and redox properties in correlation with the high catalytic activities of Ag/α–MnO_2NRs compositions. From XPS, Mn 2p, and O 1 s spectra for the MnO_2NRs and Ag/α–MnO_2NRs were used to evaluate the surface chemical characteristics of the as–prepared materials (Fig. 3). As determined by the assigned peak areas, the proportion of low valence electrons of Mn (Mn^{3+}/Mn^{4+}) followed in the sequence: 1Ag/α–MnO_2NRs (71.2%) > α–MnO_2NRs (28.8%), which is an indication of a higher number of surface oxygen vacancies (O_v) (Table S2) [42].

In particular, the amount of low valence of Mn increased to ~ 71.2% after the introduction of AgNPs in 1Ag/α–MnO_2NRs catalytic system (*i.e.,* from 28.8 to 72.2%) due to enhanced electron density, which enables in the formation of more surface oxygen vacancies were produced. Further, the increased Mn^{3+} percentage in 1Ag/MnO_2NRs was confirmed by the calculating the surface atomic molar ratios of Mn^{3+}/Mn^{4+} and found to highest Mn^{3+} species compare to other counterparts (see table S2). From Fig. 3d, the O1s spectra of the samples could be separated into two peaks, each of which represented a different oxygen species, such as lattice oxygen (O_L) of MnO_2 and adsorbed surface oxygen species ($O_{ads.}$) over MnO_2. Particularly, the peak at ca. 531.4–531.5 eV binding energies was assigned to the adsorbed surface oxygen species ($O_{ads.}$), and the peak at ca. 529.9–530.0 eV was corresponding to the lattice oxygen (O_L) of MnO_2 [42,50]. In general, surface oxygen vacancies (O_v) over MnO_2 preferentially adsorbed or activated by gaseous oxygen, hence forming the surface oxygen species ($O_{ads.}$). As a result, the content of ($O_{ads.}$) was directly correlated with the surface oxygen vacancies and had significant role catalytic performance of MnO_2 based catalysts in BnOH oxidation [42,51]. The relative concentrations of ($O_{ads.}$) species and the proportion of ($O_{ads.}$) are shown in Table S2 in the following order: MnO_2NRs (34.2) vs. 1Ag/α–MnO_2NRs (65.8) indicating the high presence of surface oxygen vacancies over AgNPs loaded catalyst. This is further confirmed by measuring the ratio of ($O_{ads.}$)/(O_L). Thus, it is evident that the ratio is relatively increased over 1Ag/MnO_2NRs compared to other catalysts (see Table S2). Additionally, the binding energy of lattice oxygen species (O_L) over MnO_2NRs was shifted from 530.0 eV to 529.5 eV for 1Ag/α–MnO_2NRs, thus, signifying an increasing electronic density around O_L, suggesting that the 1Ag/α–MnO_2NRs catalyst had more O vacancies. In addition, the Raman spectra of MnO_2NRs and 1Ag/α–MnO_2NRs are shown in Fig. 3b. It is important to note that after Ag doping the significant drop in the peaks intensity at 635 cm^{-1} was observed, which could be attributed to the increased concentration of oxygen vacancies [42,43]. Interestingly, the results observed while correlating with H_2–TPR results with the rate of BnOH conversion over various Ag loading samples was determined. The total H_2 consumption values of MnO_2NRs decreases with Ag loading (from 0.5 to 1 wt%), when further increasing the Ag loading (to 1.5%) the hydrogen consumption value is increased (Fig. 9a and Table S3). Moreover, the high reaction rate was gained at lower hydrogen consumption catalysts (*i.e.*, for 1Ag/MnO_2NRs). One can understand from this correlation that up to 1% Ag loading, the metal support interactions between Ag and MnO_2NRs is greatly enhanced and it is evident in generating higher oxygen vacancies over Ag loaded catalysts. Thus, efficient, and easier reduction of MnO_2NRs to lower oxidation state was exhibited due to H_2 spill over effect from AgNPs.

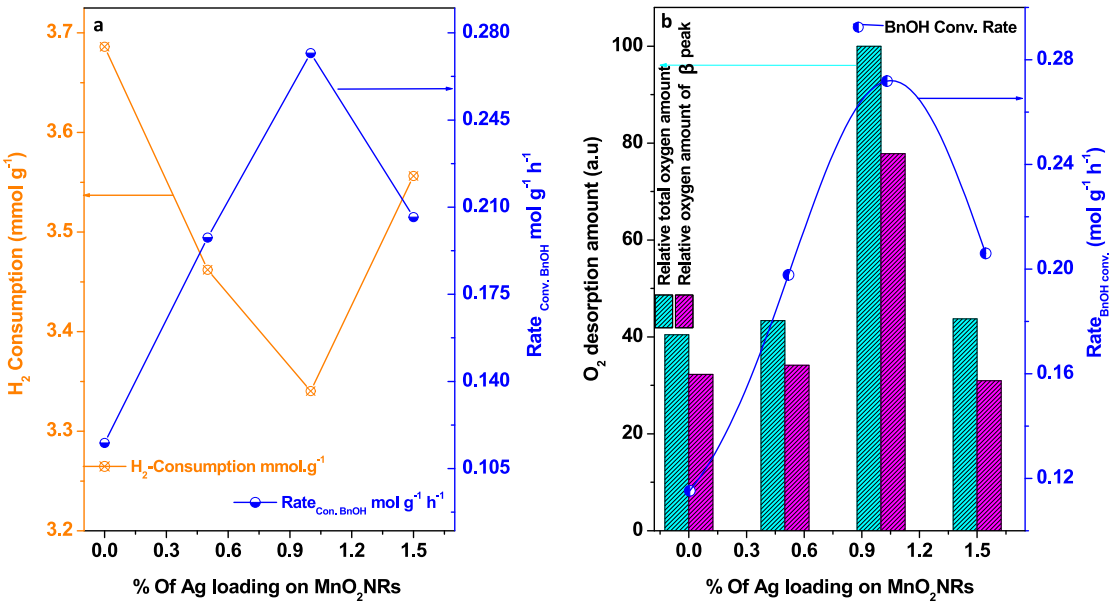

Fig. 9. Correlation of activity by a) H_2 consumption by TPR and b) O_2 desorption by TPD results with the rate of BnOH conversion with respect to Ag loadings.

Further, this can be confirmed and substantiated by correlating with O_2–TPD results. While increasing the Ag loading (from 0.5 to 1%) the oxygen desorption ability (from crystal lattice oxygen (Oβ) of MnO_2NRs is greatly increased. It reaches highest desorption value for 1Ag/MnO_2NRs sample. Denoting an increased Ov over MnO_2NRs crystal lattice for the 0.5 and 1% Ag loaded catalysts. Further increasing the Ag loading (1.5% Ag) the oxygen desorption ability of MnO_2 crystal lattice decreases due to the saturation of the Ag dispersion on MnO_2NRs surface. Overall, the highest lattice oxygen desorption (Oβ) was observed over 1Ag/MnO_2NRs catalyst and exhibiting highest rate of BnOH conversion.

Additionally, the HRTEM image of 1Ag/α–MnO_2NRs showed the

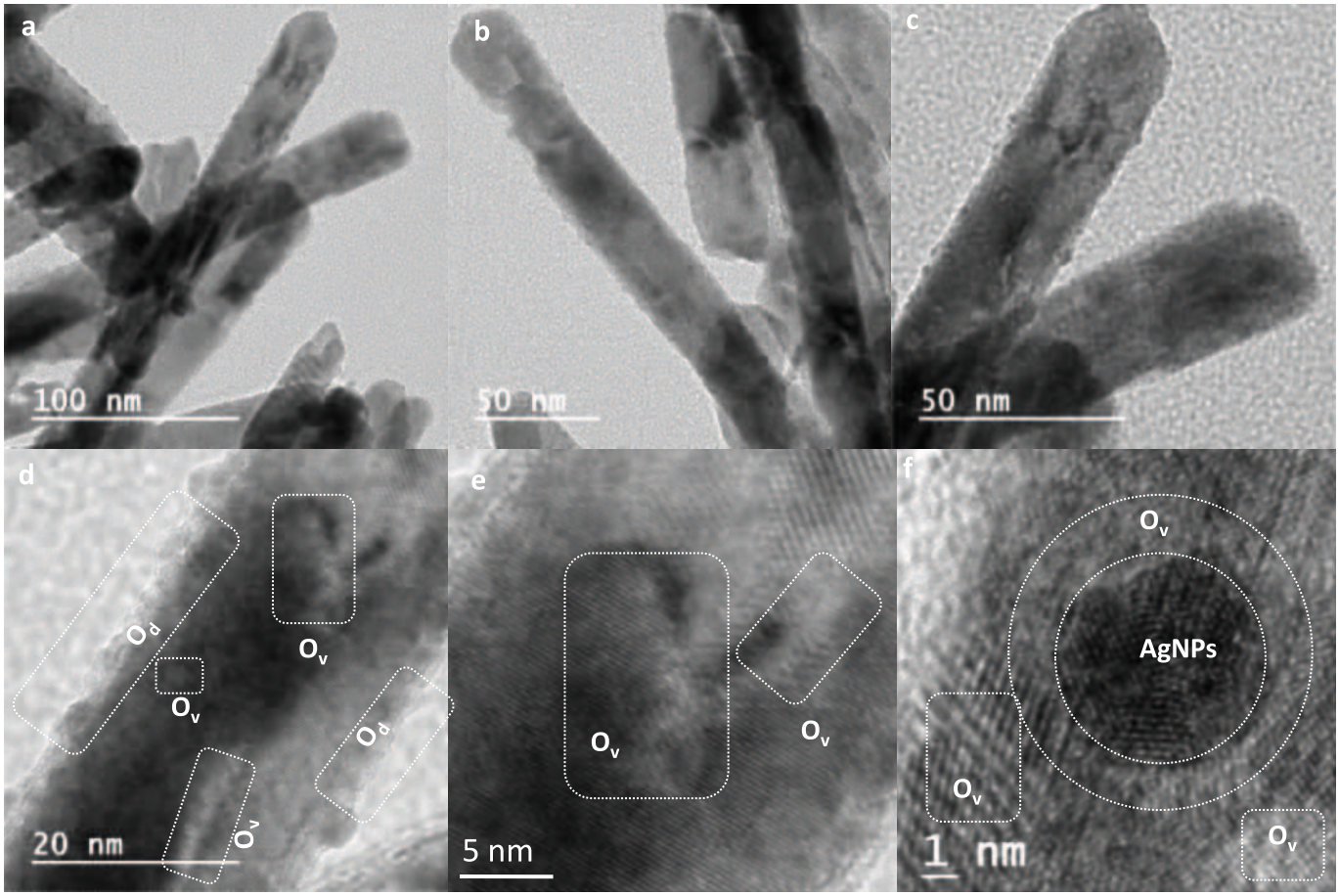

Fig. 10. (a–f) HRTEM images of highly visible oxygen vacancies on the 1Ag/α–MnO_2NRs catalyst. The Ov on MnO_2 surface presence at the proximity of AgNPs.

bulk oxygen defects. The lack of oxygen over the surface of the materials cause the bulk defects to submerge [30,52–55]. This phenomenon was noticed from HRTEM images, which increased the surface oxygen defects over 1Ag/α–MnO_2NRs catalysts (Fig. 10 a–f). HRTEM images (a–c) shows low magnification images of 1Ag/α–MnO_2NRs, it is evident from these images that the smooth and well inclined nanorods (NRs) structure converted into rough surfaces. This surface roughness might be due to the creation of oxygen vacancies over the 1Ag/α–MnO_2NRs during the calcination. Further, it can be evidently confirmed with the higher imaginations of HRTEM images (Fig. 10 d–f). It is highly visible from Fig. 10d, that the edges and the surface of the nanorods tuned into rough due to the oxygen diffusion (O_d) or oxygen liberation during calcination. Further, it is also noticed from Fig. 10 (e, f) that the disconnected lattice fringes in the HRTEM images of 1Ag/α–MnO_2NRs is highly visible, and this may be due to the formation of oxygen vacancies (O_v) on the MnO_2NRs crystal structure.

3.3. Drift study

DRIFT spectra of BnOH oxidation at 180 to 300 °C over 1Ag/MnO_2NRs and MnO_2NRs was analysed and shown in Fig. 11. DRIFT spectra were used to investigate the functional groups transformation during oxidation reaction mechanism. As shown in Fig. 11 (a–d), the spectra for 1Ag/MnO_2NRs and MnO_2NRs were almost similar during BnOH oxidation, which suggested that the reaction pathways of BnOH oxidation over MnO_2NRs based catalysts was not affected by Ag doping. Over MnO_2NRs catalysts, reaction at studied various temperature region, the main and strong bands were appeared at 1428, 1333, and 1606 cm^{-1}, these bands assigned to bending modes of $–CH_2$, −OH and stretching mode of aromatic C = C functional groups, respectively. It is clear indication that BnOH was not completely oxidized even up to 300 °C in presence of air [42,56].

However, at higher temperatures *i.e.,* 260–300 °C (Fig. 11b) a new additional carbonyl (−C = O) stretching vibrational peak appeared at 1713 cm^{-1}, and this peak indicates the partial oxidation of BnOH to benzaldehyde (BnZA). In contrast, over 1Ag/MnO_2NRs catalyst in the presence of air, few changes were observed from in situ DRIFTS spectra (Fig. 11c, d). The main and strong bands at 1359 cm^{-1} correspond to –CH bending mode, and 1583 cm^{-1} for aromatic (C = C), and 1725 cm^{-1} for (C = O) carbonyl group of the BnZA were presented. It is visible that the aromatic C = C peak was shifted to lower region for 1Ag/MnO_2NRs catalysts then MnO_2NRs this is due to the conjugation of BnZA. In addition, there are no –OH bending vibration peak was observed, interestingly, at higher temperature region (260–300 °C) the peak intensity of strong carbonyl group (–C = O) increased (Fig. 11 d), thus, it indicates the complete formation of BnZA was evident. DRIFT analysis results confirm the BnOH oxidized to BnZA at 260 °C with complete conversion over 1Ag/MnO_2NRs catalyst. In contrasts for MnO_2NRs catalyst, still unreacted BnOH was presented even at 300 °C. This observation is well correlated and substantiated with the experimental results. The observed stretching and bending vibrational peaks of BnOH and BnZA for the 1Ag/MnO_2NRs and MnO_2NRs catalysts are summarized in the table S5.

3.4. DFT results

To investigate the possible adsorption of Benzyl Alcohol on the MnO_2 surface both with and without the presence of Ag, we have calculated the binding energy. The adsorption energies are calculated in each case to understand the effect of the Ag atom in the energetics. The optimized geometries are presented in Fig. 12. A Gamma centered K grid is used for the Brillouin zone integration and a plane wave kinetic energy cut–off of 520 eV is used. Generalized gradient approximation (GGA) is employed for exchange and correlation interactions and PAW–PBE pseudo potentials are used [33,34].

The E_{ads} = adsorption(binding) energy is calculated by the formula,

$$E_{ads} = E_{(MnO2+adsorbate)} - - E_{MnO2} - - \mu(adsorbate) \quad (1)$$

where, $E_{(MnO2+adsorbate)}$ is the total energy of the MnO_2 surface with adsorbate on it, E_{MnO2} is the total energy of the bare surface and μ

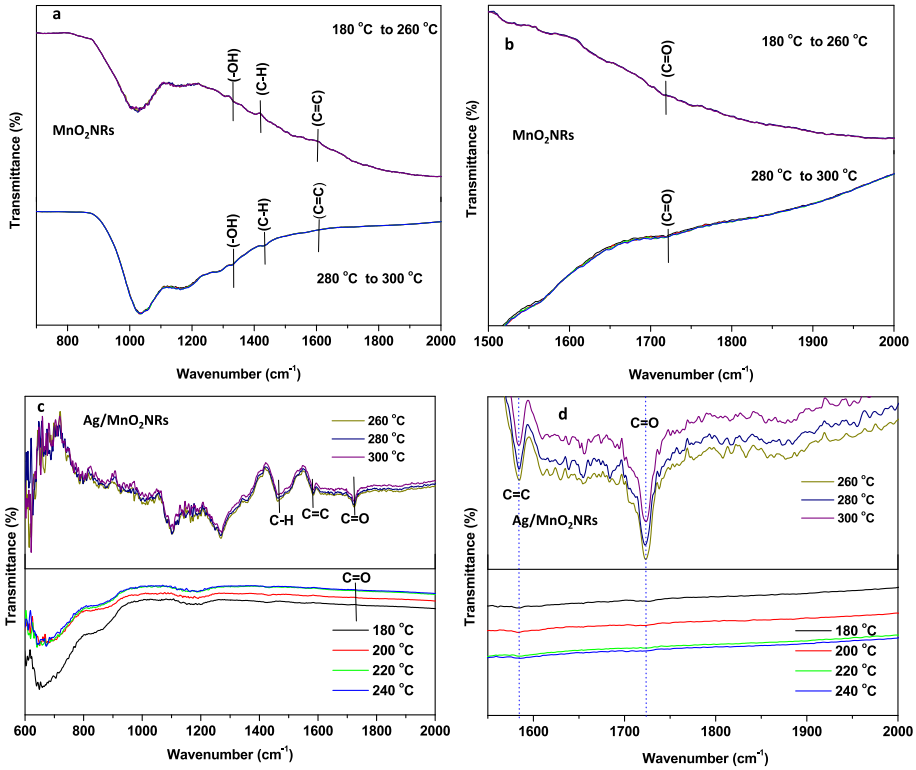

Fig. 11. DRIFT spectra of BnOH dosed catalysts (a, b) MnO_2NRs and (c,d) 1Ag/MnO_2NRs for various temperature (180 °C to 300 °C) in presence of air.

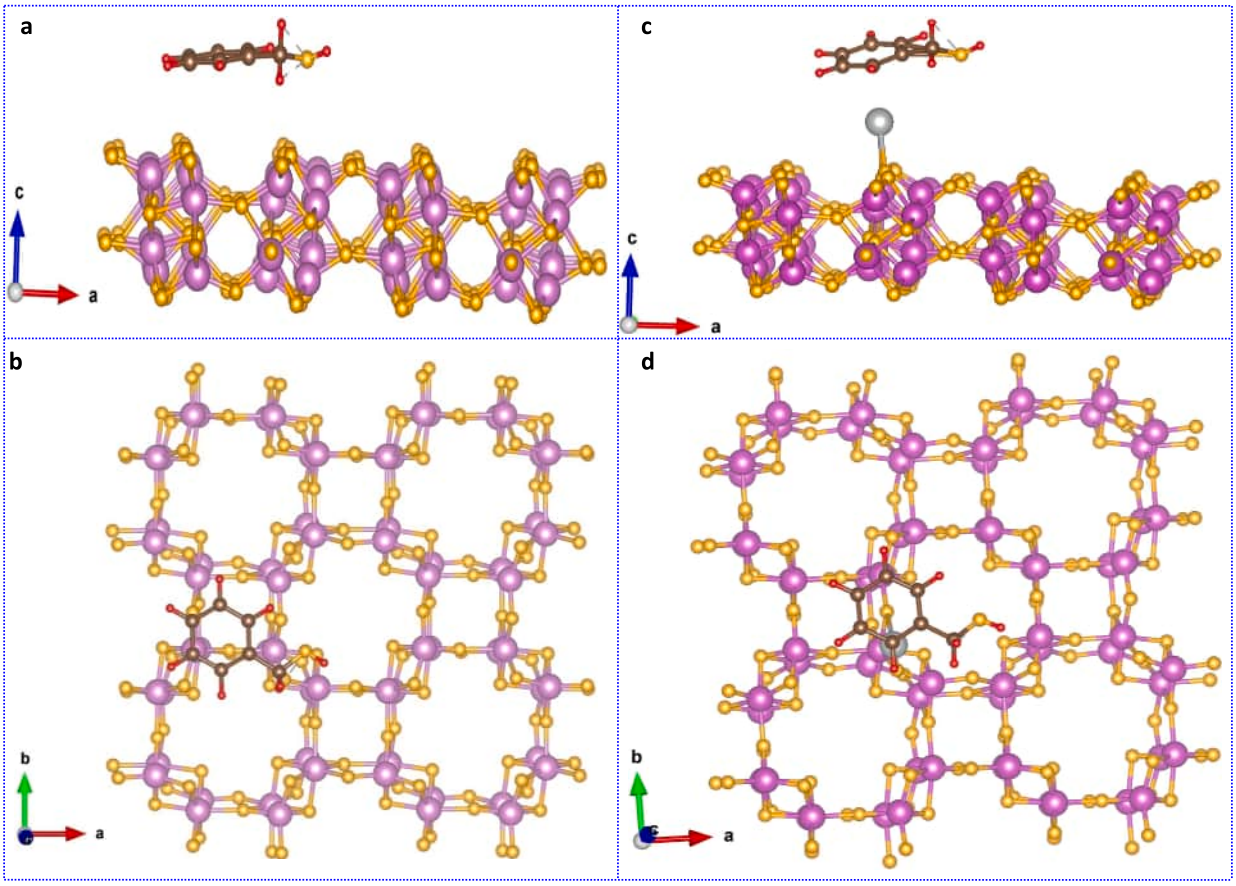

Fig. 12. (a, b) The top and side views of the MnO_2 surface with Benzyl Alcohol adsorbed on top of it. Color codes of the atoms are purple: Mn, golden: O, red: H and brown: C. Fig. 1(c, d). The top and side views of the MnO_2 + Ag surface with Benzyl Alcohol adsorbed on top of it. Color codes of the atoms are, purple: Mn, golden: O, red: H and brown: C and silver: Ag. (For interpretation of the references to color in this figure legend, the reader is referred to the web version of this article.)

Table 3
Surface binding energies of the benzyl alcohol adsorption on two surfaces.

Configuration	Binding energy (eV)	Distance of molecule from surface (Å)
MnO_2 + BnOH	–0.043	2.41
MnO_2 + Ag + BnOH	–1.43	2.29

(adsorbate) is the single point energy (chemical potential) of the adsorbate, which is BnOH in this case. The single point energy of BnOH is calculated as the total energy of the molecule calculated by putting it in a box of dimensions 15x15x15 Ang^3. The calculated adsorption energies are presented in Table 3.

The negative adsorption energy indicates that the reaction is exothermic and is energetically favorable. The calculated binding energy of BnOH to the MnO_2 surface is –0.043 eV, and the binding energy is reduced to –1.43 eV when it is adsorbed in presence of the Ag atom at the surface. Furthermore, the distance of BnOH molecules to the surface is reduced from 2.41 Å to 2.29 Å in presence of Ag. These findings indicate that Ag is a favorable adsorbate at the MnO_2 surface that helps to bind the BA molecule strongly.

4. Discussion

Owing to its ability to switch between the + 4 and + 3 oxidation states, MnO_2 is a versatile oxidation catalyst support. Moreover, MnO_2 phase and the crystal structure had variable activities in the oxidation reactions. The preparation methods and the conditions are highly influential on the formation of crystal structures of MnO_2 such as α, β, γ, and δ phases. Moreover, each phase had distinctive properties in exhibiting the different amount of oxygen vacancies, surface adsorption energies, and unsaturated Mn environment [28]. The structure sensitivity and the correlation with the oxidation activity are highly reported in the literature. Herein, the structure with shaped controlled active Ag nanoparticles is well correlated with the oxygen activation. It is substantiated that the MnO_2 support alone is not sufficient to achieve higher oxidation activity.

The catalytic activity of the active component that has been dispersed on a suitable support is significantly higher than that of the bulk support (for example, a noble metal dispersed on an oxide support). Therefore, one efficient method to increase the catalytic activity of MnO_2 is to decorate with a noble metal with low loadings. The main objective of this research is to increase the surface oxidation properties of MnO_2 and to understand how the addition of AgNPs catalysts enhances the MnO_2 activity. In an attempt to determine the actual required of AgNPs, bare AgNPs were used in a BnOH oxidation reaction, which yielded no oxidation activity. On the other hand, when we added AgNPs over MnO_2 surface, the outcome of the BnOH oxidation was improved greatly. It is confirmed that AgNPs have a significant impact on MnO_2 activity, and as a result, it is concluded that the oxidation step of BnOH takes place mostly on the Ag–MnO_2 surface interface of the catalysts (Scheme 2). The BnOH conversion rate of pure α–MnO_2NRs is 0.1043 mol $g^{-1}h^{-1}$. Interestingly, the rate of conversion reached as high as 0.2719 mol $g^{-1}.h^{-1}$ upon incorporation of 1 wt% AgNPs loading on the α–MnO_2NRs. Thus, the catalytic activity of α–MnO_2NRs with 1% AgNPs decoration is increased by 2.6 times when compared to the activity of pure α–MnO_2NRs, which is profoundly high values compared to the reported values. The low activity of α–MnO_2NRs is also indicated by the

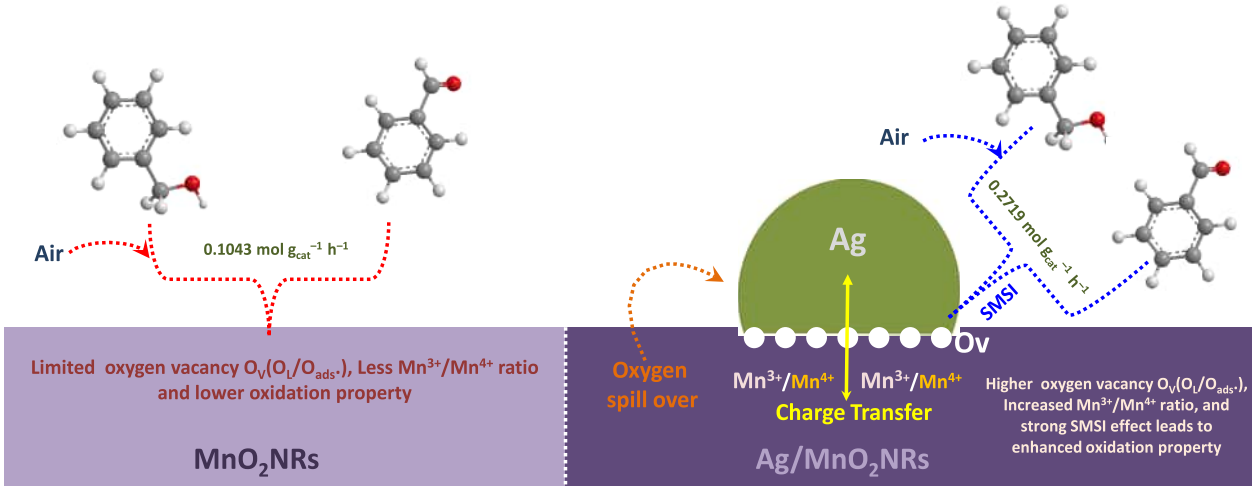

Scheme 2. The plausible mechanism of partial oxidation of BnOH to BnZA over MnO_2NRs and Ag/MnO_2NRs catalysts.

limited redox activity at low temperature as compared to that of 1Ag/α–MnO_2NRs. The enhancement of the BnOH oxidation activity of Ag/MnO_2NRs catalysts is mainly due to increase redox ability (Mn^{3+}/Mn^{4+}), strong metal support interaction (SMSI) and increased oxygen vacancy (O_v) leads to Mars–van–Krevelen (Scheme 2). In addition, the size of the α–MnO_2NRs particles were also calculated from the TEM and HRTEM microscopic analysis and displayed a similar in size even after AgNPs loading (1Ag/α–MnO_2NRs). Thus, indicating that the reaction is not depending on the size of the MnO_2NRs. Furthermore, interesting results were noticed from the HRTEM images in Fig. 10. We discovered that the more oxygen vacancies and defects creation on the α–MnO_2NRs was evident and visible over the rough surfaces after the AgNPs incorporation. Over MnO_2NRs surface displayed a smooth and shiny surface by microscopic imaging and thus, it confirms the low lattice oxygen vacancies. The detailed discussed characterisation results such as XPS, O_2-TPD, Raman, and HRTEM clearly confirming the 1Ag/α–MnO_2NRs catalyst exhibiting the highest oxygen vacancies, and the strong metal-support interactions between AgNPs and MnO_2NRs was confirmed with H_2–TPR, FT–IR, XPS and HRTEM.

5. Conclusions

In summary, morphologically designed and prepared uniform AgNPs with the mean size of ~ 6 nm and the α-MnO_2 nanorods (NRs) with diameter of ~ 25 nm was prepared separately. The pre–synthesised AgNPs were decorated on the MnO_2NRs by simple impregnated method to evaluate the catalytic activity in selective oxidation of benzyl alcohol (BnOH) in vapor phase conditions. Compared with the synthesized MnO_2NRs catalyst support materials, the incorporated Ag nanoparticles into α–MnO_2NRs catalysts exhibited enhanced activity in BnOH oxidation. Experimentally and computationally, it is concluded that the benzyl alcohol molecule binds strongly over Ag/MnO_2 than bare MnO_2. The optimised catalyst (1Ag/α–MnO_2NRs) shown superior performance with the reaction rate of 0.2719 (mol $g^{-1}h^{-1}$) at highest WHSV (28.5 h^{-1}) value at 260 °C, This result is 2.6 times higher than the reported values in the literature. A series of techniques were used to characterise the as–prepared catalysts demonstrated that the enhanced catalytic performance of 1Ag/α–MnO_2NRs were closely associated with the increased oxygen vacancies (*i.e.,* increased active oxygen species) on the α–MnO_2NRs and strong metal support interactions led high surface adsorption energy. Ag doped α–MnO_2NRs catalyst is a robust catalyst for BnOH oxidation due to uniform AgNPs highly anchored on MnO_2NRs support. Novel designed AgNPs can further impregnate over various solid carrier materials (metal oxides, polymers, carbon-based materials, etc.,) and it may provide an alternative strategy for catalyst development for other applications.

Declaration of Competing Interest

The authors declare that they have no known competing financial interests or personal relationships that could have appeared to influence the work reported in this paper.

Data availability

Data will be made available on request.

Acknowledgements

Dr. Prem Kumar Seelam acknowledges the Hycat3 project and Hycamite Oy, Finland. P. Vijayanand greatly acknowledges to TSP–0202 project for funding in CSIR-Indian Institute of Chemical Technolgies, Hyderabad, India. This research was supported by Chungnam National University (2021–2022) for DRIFT analysis. Dr. Assa Aravindh wish to acknowledge CSC – IT Center for Science, Finland, for computational resources in DFT calculations.

Appendix A. Supplementary data

Supplementary data to this article can be found online at https://doi.org/10.1016/j.cej.2023.144007.

References

[1] C.M. Crombie, R.J. Lewis, R.L. Taylor, D.J. Morgan, T.E. Davies, A. Folli, D. M. Murphy, J.K. Edwards, J. Qi, H. Jiang, C.J. Kiely, X. Liu, M.S. Skjøth-Rasmussen, G.J. Hutchings, Enhanced selective oxidation of benzyl alcohol via in situ H_2O_2 production over supported Pd–based catalysts, ACS Catal. 11 (2021) 2701–2714, https://doi.org/10.1021/acscatal.0c04586.

[2] J. Wang, H. Liang, C. Zhang, B. Jin, Y. Men, Bi_2WO_6-x nanosheets with tunable Bi quantum dots and oxygen vacancies for photocatalytic selective oxidation of alcohols, Appl. Catal. B: Environ. 256 (2019), 117874, https://doi.org/10.1016/j.apcatb.2019.117874.

[3] F. Xu, J. Wang, N. Zhang, H. Liang, H. Sun, Simultaneously generating Bi quantum dot and oxygen vacancy on Bi_2MoO_6 nanosheets for boosting photocatalytic selective alcohol oxidation, Appl. Surf. Sci. 575 (2022), 151738, https://doi.org/10.1016/j.apsusc.2021.151738.

[4] C. Meng, K. Yang, X. Fu, R. Yuan, Photocatalytic oxidation of benzyl alcohol by homogeneous $CuCl_2$/solvent: a model system to explore the role of molecular oxygen, ACS Catal. 5 (2015) 3760–3766, https://doi.org/10.1021/acscatal.5b00644.

[5] E. Nikoloudakis, P.B. Pati, G. Charalambidis, D.S. Budkina, S. Diring, A. Planchat, D. Jacquemin, E. Vauthey, A.G. Coutsolelos, F. Odobel, Dye-sensitized photoelectrosynthesis cells for benzyl alcohol oxidation using a zinc porphyrin

sensitizer and TEMPO catalyst, ACS Catal. 11 (2021) 12075–12086, https://doi.org/10.1021/acscatal.1c02609.
[6] T. Mallat, A. Baiker, Oxidation of alcohols with molecular oxygen on solid catalysts, Chem Rev. 104 (2004) 3037–3058, https://doi.org/10.1021/cr0200116.
[7] A. Abad, P. Concepción, A. Corma, H. García, A collaborative effect between gold and a support induces the selective oxidation of alcohols, Angew. Chemie-Int. Ed. 44 (2005) 4066–4069, https://doi.org/10.1002/anie.200500382.
[8] V.R. Choudhary, A. Dhar, P. Jana, R. Jha, B.S. Uphade, A green process for chlorine-free benzaldehyde from the solvent-free oxidation of benzyl alcohol with molecular oxygen over a supported nano–size gold catalyst, Green Chem. 7 (2005) 768–770, https://doi.org/10.1039/b509003b.
[9] R.B. Tosun, K.Ö. Hamaloğlu, P.A. Kavaklı, C. Kavaklı, A. Tuncel, A synergistic catalyst based on a multivalence monodisperse-porous microspheres with oxygen vacancies for benzyl alcohol oxidation, Molecular Catalysis 497 (2020), 111227, https://doi.org/10.1016/j.mcat.2020.111227.
[10] X. Li, J. Wang, Y. Men, Z. Bian, TiO_2 mesocrystal with exposed (001) facets and CdS quantum dots as an active visible photocatalyst for selective oxidation reactions, Appl. Catal. B: Environ. 187 (2016) 115–121, https://doi.org/10.1016/j.apcatb.2016.01.034.
[11] J. Wang, Z. Chen, G. Zhai, Y. Men, Boosting photocatalytic activity of WO_3 nanorods with tailored surface oxygen vacancies for selective alcohol oxidations, Appl. Surf. Sci. 462 (2018) 760–771, https://doi.org/10.1016/j.apsusc.2018.08.181.
[12] D. Li, J. Wang, F. Xu, N. Zhang, Y. Men, Mesoporous (001)–TiO_2 nanocrystals with tailored Ti3+ and surface oxygen vacancies for boosting photocatalytic selective conversion of aromatic alcohols, Catal. Sci. Technol. 11 (2021) 2939–2947, https://doi.org/10.1039/D1CY00053E.
[13] L. Jia, S. Zhang, F. Gu, Y. Ping, X. Guo, Z. Zhong, F. Su, Highly selective gas-phase oxidation of benzyl alcohol to benzaldehyde over silver-containing hexagonal mesoporous silica, Microporous Mesoporous Mater. 149 (2012) 158–165, https://doi.org/10.1016/j.micromeso.2011.08.009.
[14] D. Han, T. Xu, J. Su, X. Xu, Y. Ding, Gas-phase selective oxidation of benzyl alcohol to benzaldehyde with molecular oxygen over unsupported nanoporous gold, ChemCatChem 2 (2010) 383–386, https://doi.org/10.1002/cctc.201000001.
[15] J. Fan, Y. Dai, Y. Li, N. Zheng, J. Guo, X. Yan, G.D. Stucky, Low-temperature, highly selective, gas-phase oxidation of benzyl alcohol over mesoporous K-Cu–TiO_2 with stable copper(I) oxidation state, J. Am. Chem. Soc. 131 (2009) 15568–15569, https://doi.org/10.1021/ja9032499.
[16] J. Mao, M. Deng, Q. Xue, L. Chen, Y. Lu, Thin-sheet Ag/Ni–fiber catalyst for gas-phase selective oxidation of benzyl alcohol with molecular oxygen, Catal. Commun. 10 (2009) 1376–1379, https://doi.org/10.1016/j.catcom.2009.03.006.
[17] Y.S. Sawayama, H. Shibahara, Y. Ichihashi, S. Nishiyama, S. Tsuruya, Promoting effect and role of alkaline earth metal added to supported Ag catalysts in the gas–phase catalytic oxidation of benzyl alcohol, Ind. Eng. Chem. Res. 45 (2006) 8837–8845, https://doi.org/10.1021/ie061091x.
[18] D. Nakashima, Y. Ichihashi, S. Nishiyama, S. Tsuruya, Promoted partial oxidation activity of alkali metal added-Co catalysts supported on NaY and NaUSY zeolites in the gas–phase catalytic oxidation of benzyl alcohol, J. Mol. Catal. A Chem. 259 (2006) 108–115, https://doi.org/10.1016/j.molcata.2006.05.068.
[19] R. Yamamoto, Y.S. Sawayama, H. Shibahara, Y. Ichihashi, S. Nishiyama, S. Tsuruya, Promoted partial oxidation activity of supported Ag catalysts in the gas-phase catalytic oxidation of benzyl alcohol, J. Catal. 234 (2005) 308–317, https://doi.org/10.1016/j.jcat.2005.06.032.
[20] A. Kumar, V.P. Kumar, B.P. Kumar, V. Vishwanathan, K.V.R. Chary, Vapor phase oxidation of benzyl alcohol over gold nanoparticles supported on mesoporous TiO2, Catal. Letters. 144 (2014) 1450–1459, https://doi.org/10.1007/s10562-014-1285-6.
[21] W. Lewandowski, M. Fruhnert, J. Mieczkowski, C. Rockstuhl, E. Górecka, Dynamically self–assembled silver nanoparticles as a thermally tunable metamaterial, Nat. Commun. 6 (2015), https://doi.org/10.1038/ncomms7590.
[22] L. Gurrala, A.S. Nagpure, H.R. Gurav, S. Chilukuri, Spinel-type mixed oxides for stable and selective partial oxidation of benzyl alcohol, ChemistrySelect 3 (2018) 3751–3761, https://doi.org/10.1002/slct.201800321.
[23] T. Mazumder, S. Dandapat, T. Baidya, P.R. Likhar, A.H. Clark, P. Bera, K. Tiwari, S. Payra, B. Srinivasa Rao, S. Roy, K. Biswas, Dual-site cooperation for high benzyl alcohol oxidation activity of MnO_2 in biphasic MnOx-CeO_2 catalyst using aerial O_2 in the vapor phase, J. Phys. Chem. C. 125 (2021) 20831–20844, https://doi.org/10.1021/acs.jpcc.1c04158.
[24] C. Della Pina, E. Falletta, M. Rossi, Highly selective oxidation of benzyl alcohol to benzaldehyde catalyzed by bimetallic gold–copper catalyst, J. Catal. 260 (2008) 384–386, https://doi.org/10.1016/j.jcat.2008.10.003.
[25] S. Balgooyen, P.J. Alaimo, C.K. Remucal, M.G. Vogel, Structural transformation of MnO_2 during the oxidation of bisphenol A, Environ. Sci. Technol. 51 (11) (2017) 6053–6062, https://doi.org/10.1021/acs.est.6b05904.
[26] S. Dey, N.S. Mehta, Selection of Manganese oxide catalysts for catalytic oxidation of carbon monoxide at ambient conditions, Resources Environment and Sustainability 1 (2020), 100003, https://doi.org/10.1016/j.resenv.2020.100003.
[27] M. Villalobos, B. Toner, J. Bargar, G. Sposito, Characterization of the manganese oxide produced by Pseudomonas putida strain MnB1, Geochim. Cosmochim. Acta 67 (14) (2003) 2649–2662, https://doi.org/10.1016/S0016-7037(03)00217-5.
[28] J. Shi, T. Qi, B.-C. Sun, G.-W. Chu, J.-F. Chen, Catalytic oxidation of benzyl alcohol over MnO_2: structure-activity description and reaction mechanism, Chem Eng. J. 440 (2022) 135802.
[29] Z. Wang, Z. Wang, W. Li, Y. Lan, C. Chen, Performance comparison and mechanism investigation of Co_3O_4–modified different crystallographic MnO_2 (α, β, γ, and δ) as an activator of peroxymonosulfate (PMS) for sulfisoxazole degradation, Chem Eng. J. 427 (2022) 130888.
[30] W. Yang, Z. Su, Z. Xu, W. Yang, Y. Peng, J. Li, Comparative study of α–, β–, γ- and δ–MnO_2 on toluene oxidation: oxygen vacancies and reaction intermediates, Appl. Catal. B Environ. 260 (2020) 118150.
[31] R. Rajesh, P. Arunkumar, B. Putrakumar, R. Venkatesan, Self-assembled uniform silver nanoparticles (SAAgNPs) and their supported MoO_3 nanocatalysts for effective degradation of azo dyes, ChemistrySelect 4 (2019) 10770–10776, https://doi.org/10.1002/slct.201902318.
[32] R. Rajendiran, A. Patchaiyappan, S. Harisingh, P. Balla, A. Paari, B. Ponnala, V. Perupogu, U. Lassi, P.K. Seelam, Synergistic effects of graphene oxide grafted chitosan & decorated MnO_2 nanorods composite materials application in efficient removal of toxic industrial dyes, J. Water Process Eng. 47 (2022), https://doi.org/10.1016/j.jwpe.2022.102704.
[33] G. Kresse, J. Hafner, Ab. initio molecular dynamics for liquid metals, Phys. Rev. B 47 (1) (1993) 558–561.
[34] G. Kresse, D. Joubert, From ultrasoft pseudopotentials to the projector augmented-wave method, Phys. Rev. B 59 (3) (1999) 1758–1775.
[35] J.P. Perdew, K. Burke, M. Ernzerhof, Generalized gradient approximation made simple, Phys. Rev. Lett. 77 (18) (1996) 3865–3868.
[36] P.E. Blöchl, Projector augmented-wave method, Phys. Rev. B 50 (24) (1994) 17953–17979.
[37] N. Zheng, J. Fan, G.D. Stucky, One-step one–phase synthesis of monodisperse noble-metallic nanoparticles and their colloidal crystals, J. Am. Chem. Soc. 128 (2006) 6550–6551, https://doi.org/10.1021/ja0604717.
[38] R. Sato, M. Kanehara, T. Teranishi, Homoepitaxial size control and large–scale synthesis of highly monodisperse amine-protected palladium nanoparticles, Small 7 (2011) 469–473, https://doi.org/10.1002/smll.201001685.
[39] Z. Li, J. Gao, X. Xing, S. Wu, S. Shuang, C. Dong, M.C. Paau, M.M.F. Choi, Synthesis and characterization of n–alkylamine–stabilized palladium nanoparticles for electrochemical oxidation of methane, J. Phys. Chem. C. 114 (2010) 723–733, https://doi.org/10.1021/jp907745v.
[40] L. Zhang, W. Niu, G. Xu, Seed-mediated growth of palladium nanocrystals: The effect of pseudo-halide thiocyanate ions, Nanoscale 3 (2011) 678–682, https://doi.org/10.1039/c0nr00622j.
[41] G. Xu, Y. Zhang, J. Lin, Y. Wang, X. Shi, Y. Yu, H. He, Unraveling the mechanism of ammonia selective catalytic oxidation on Ag/Al_2O_3catalysts by operando spectroscopy, ACS Catal. 11 (2021) 5506–5516, https://doi.org/10.1021/acscatal.1c01054.
[42] L. Zhang, S. Zhu, R. Li, W. Deng, C. Hong, D. Liu, L. Guo, Ag–doped δ–mno_2nanosheets as robust catalysts for toluene combustion, ACS Appl. Nano Mater. 3 (2020) 11869–11880, https://doi.org/10.1021/acsanm.0c02444.
[43] V. Sannasi, K. Subbian, Influence of Moringa oleifera gum on two polymorphs synthesis of MnO_2 and evaluation of the pseudo–capacitance activity, J. Mater. Sci. Mater. Electron. 31 (2020) 17120–17132, https://doi.org/10.1007/s10854-020-04272-z.
[44] D. Shu, C. He, H. Yi, A. Gao, X. Pang, Z. Ao, S. Deng, F. Yi, X. Zhou, Z. Zhu, Preparation of single–atom Ag-decorated MnO_2 hollow microspheres by redox etching method for high-performance solid–state asymmetric supercapacitors, ACS Appl. Energy Mater. 3 (2020) 10192–10201, https://doi.org/10.1021/acsaem.0c01969.
[45] E. Hayashi, Y. Yamaguchi, K. Kamata, N. Tsunoda, Y. Kumagai, F. Oba, M. Hara, Effect of MnO_2 crystal structure on aerobic oxidation of 5–hydroxymethylfurfural to 2,5–furandicarboxylic acid, J. Am. Chem. Soc. 141 (2019) 899–900, https://doi.org/10.1021/jacs.8b09917.
[46] H. Deng, S. Kang, J. Ma, C. Zhang, H. He, Silver incorporated into cryptomelane–type manganese oxide boosts the catalytic oxidation of benzene, Appl. Catal. B Environ. 239 (2018) 214–222, https://doi.org/10.1016/j.apcatb.2018.08.006.
[47] S. Lu, X. Wang, Q. Zhu, C. Chen, X. Zhou, F. Huang, K. Li, L. He, Y. Liu, F. Pang, Ag–K/MnO_2 nanorods as highly efficient catalysts for formaldehyde oxidation at low temperature, RSC Adv. 8 (2018) 14221–14228, https://doi.org/10.1039/c8ra01611a.
[48] N.N. Opembe, C. Guild, C. King'ondu, N.C. Nelson, I.I. Slowing, S.L. Suib, Vapor-phase oxidation of benzyl alcohol using manganese oxide octahedral molecular sieves (OMS–2), Ind. Eng. Chem. Res. 53 (49) (2014) 19044–19051.
[49] H. Hayashibara, S. Nishiyama, S. Tsuruya, M. Masai, The effect of alkali promoters on Cu–Na–ZSM–5 catalysts in the oxidation of benzyl alcohol, J. Catal. 153 (1995) 254–264, https://doi.org/10.1006/jcat.1995.1128.
[50] J. Wang, J. Li, C. Jiang, P. Zhou, P. Zhang, J. Yu, The effect of manganese vacancy in birnessite–type MnO_2 on room-temperature oxidation of formaldehyde in air, Appl. Catal. B Environ. 204 (2017) 147–155, https://doi.org/10.1016/j.apcatb.2016.11.036.
[51] X. Li, J. Ma, L. Yang, G. He, C. Zhang, R. Zhang, H. He, Oxygen vacancies induced by transition metal doping in γ–MnO_2 for highly efficient ozone decomposition, Environ. Sci. Technol. 52 (2018) 12685–12696, https://doi.org/10.1021/acs.est.8b04294.
[52] M. Han, J. Huang, S. Liang, L. Shan, X. Xie, Z. Yi, Y. Wang, S. Guo, J. Zhou, Oxygen defects in β–MnO_2 enabling high-performance rechargeable aqueous zinc/manganese dioxide battery, Science 23 (1) (2020) 100797.
[53] L.T. Tseng, Y. Lu, H.M. Fan, Y. Wang, X. Luo, T. Liu, P. Munroe, S. Li, J. Yi, Magnetic properties in α–MnO_2 doped with alkaline elements, Sci. Rep. 5 (2015), https://doi.org/10.1038/srep09094.
[54] G. Zhu, J. Zhu, W. Li, W. Yao, R. Zong, Y. Zhu, Q. Zhang, Tuning the K^+ concentration in the tunnels of α–MnO_2 to increase the content of oxygen vacancy

for ozone elimination, Environ. Sci. Technol. 52 (2018) 8684–8692, https://doi.org/10.1021/acs.est.8b01594.

[55] S. Ding, M. Zhang, R. Qin, J. Fang, H. Ren, H. Yi, L. Liu, W. Zhao, Y. Li, L. Yao, S. Li, Q. Zhao, F. Pan, Oxygen-deficient β–MnO_2@graphene oxide cathode for high-rate and long-life aqueous zinc ion batteries, Nano-Micro Lett. 13 (2021), https://doi.org/10.1007/s40820-021-00691-7.

[56] E. Nowicka, J.P. Hofmann, S.F. Parker, M. Sankar, G.M. Lari, S.A. Kondrat, D. W. Knight, D. Bethell, B.M. Weckhuysen, G.J. Hutchings, In situ spectroscopic investigation of oxidative dehydrogenation and disproportionation of benzyl alcohol, Phys. Chem. Chem. Phys. 15 (2013) 12147–12155, https://doi.org/10.1039/c3cp50710f.